BIOMECHANICS OF COMMON CAROTID ARTERIES FROM MICE HETEROZYGOUS FOR MgR, THE MOST COMMON MOUSE MODEL OF MARFAN SYNDROME

A Thesis

by

ANNE IRENE TAUCER

Submitted to the Office of Graduate Studies of
Texas A&M University
in partial fulfillment of the requirements for the degree of

MASTER OF SCIENCE

December 2006

Major Subject: Biomedical Engineering

BIOMECHANICS OF COMMON CAROTID ARTERIES FROM MICE HETEROZYGOUS FOR MgR, THE MOST COMMON MOUSE MODEL OF MARFAN SYNDROME

A Thesis

by

ANNE IRENE TAUCER

Submitted to the Office of Graduate Studies of
Texas A&M University
in partial fulfillment of the requirements for the degree of

MASTER OF SCIENCE

Approved by:

Co-Chairs of Committee,	Jay D. Humphrey
	Emily Wilson
Member of Committee,	Alvin T. Yeh
Head of Department,	Gerard L. Coté

December 2006

Major Subject: Biomedical Engineering

ABSTRACT

Biomechanics of Common Carotid Arteries from Mice

Heterozygous for MgR, the Most Common

Mouse Model of Marfan Syndrome. (December 2006)

Anne Irene Taucer, B.S., Texas A&M University

Co-Chairs of Committee: Dr. Jay Humphrey
Dr. Emily Wilson

Marfan syndrome, affecting approximately one out of every 5,000 people, is characterized by abnormal bone growth, ectopia lentis, and often-fatal aortic dilation and dissection. The root cause is a faulty extracellular matrix protein, fibrillin-1, which associates with elastin in many tissues. Common carotids from wild-type controls and mice heterozygous for the mgR mutation, the most commonly used mouse model of Marfan syndrome, were studied in a biaxial testing device. Mechanical data in the form of pressure-diameter and force-stretch tests in both the active and passive states were collected, as well data on the functional responses to phenylephrine, carbamylcholine chloride, and sodium nitroprusside. Although little significant difference was found between the heterozygous and wild-type groups in general, the *in vivo* stretch for both groups was significantly different from previously studied mouse vessels. Although the two groups do not exhibit significant differences, this study comprises a control group for future work with mice homozygous for mgR, which do exhibit Marfan-like symptoms. As treatment of Marfan syndrome improves, more Marfan patients will survive and age, increasing the likelihood that they will develop many of the vascular

complications affecting the normal population, including hypertension and atherosclerosis. Therefore, it is imperative to gather biomechanical data from the Marfan vasculature so that clinicians may predict the effects of vascular complications in Marfan patients and develop appropriate methods of treatment.

ACKNOWLEDGEMENTS

This research project was funded through the National Institutes of Health (NIH) grant number NIH R21 EB-4106. I would like to thank my committee, Dr. Humphrey, Dr. Wilson, and Dr. Yeh, for their direction and advice during the past two and a half years and during the preparation of this thesis. I am very grateful to Dr. Rudy Gleason and Wendy Watson for training me and to John Eberth and Kris Miller for their assistance in data collection. I would like to thank my parents, David and Penny, and my parents-in-law, Anton and Sharon, for all their support and advice. Finally, I owe a debt of gratitude to my husband, Philip, for all the reassurance, help, and encouragement he provided throughout my graduate career.

TABLE OF CONTENTS

Page

ABSTRACT iii

ACKNOWLEDGEMENTS v

TABLE OF CONTENTS vi

LIST OF FIGURES vii

LIST OF TABLES ix

INTRODUCTION 1

- Symptoms and Prognosis of Marfan Syndrome 2
- Fibrillin-1, Microfibrils, and Elastic Fibers 4
- Mouse Models of Marfan Syndrome 10
- Fibrillin and Vascular Mechanics 12

BIOMECHANICAL TESTING 16

- Materials and Methods 16
- Results 22
- Discussion 39

CONCLUSION AND RECOMMENDATIONS 45

REFERENCES 46

APPENDIX A 52

APPENDIX B 66

APPENDIX C 68

VITA 70

LIST OF FIGURES

FIGURE		Page
1	Representative functional response curves	25
2	Averaged active wild-type and heterozygous pressure-diameter curves	27
3	Averaged passive wild-type and heterozygous pressure-diameter curves	28
4	Representative active wild-type and heterozygous circumferential stress-strain curves	29
5	Representative passive wild-type and heterozygous circumferential stress-strain curves	30
6	Averaged active wild-type and heterozygous force-pressure curves	31
7	Averaged passive wild-type and heterozygous force-pressure curves	32
8	Representative active wild-type axial force-stretch curves	34
9	Representative active heterozygous axial force-stretch curves	35
10	Representative active wild-type axial stress-stretch curves	36
11	Representative active heterozygous axial stress-stretch curves	37
12	Averaged active and passive axial *in vivo* stretches and forces	38
13	Averaged pressure-diameter curves at an axial stretch of 1.65	52
14	Averaged pressure-diameter curves at an axial stretch of 1.75	53
15	Averaged pressure-diameter curves at an axial stretch of 1.85	54
16	Representative circumferential stress-stretch curves at an axial stretch of 1.65	55

FIGURE Page

17 Representative circumferential stress-stretch curves at an axial stretch of 1.75..... 56

18 Representative circumferential stress-stretch curves at an axial stretch of 1.85..... 57

19 Representative axial force-stretch curves at a pressure of 0 mmHg 58

20 Representative axial force-stretch curves at a pressure of 60 mmHg 59

21 Representative axial force-stretch curves at a pressure of 100 mmHg 60

22 Representative axial force-stretch curves at a pressure of 160 mmHg 61

23 Representative axial stress-stretch curves at a pressure of 0 mmHg..... 62

24 Representative axial stress-stretch curves at a pressure of 60 mmHg..... 63

25 Representative axial stress-stretch curves at a pressure of 100 mmHg.... 64

26 Representative axial stress-stretch curves at a pressure of 160 mmHg.... 65

LIST OF TABLES

TABLE Page

1 Comparisons of mouse and vessel properties for wild-type and heterozygous mgR mice 24

2 Comparisons of active and passive *in vivo* stretches and forces for wild-type and heterozygous mgR mice 39

INTRODUCTION

Marfan syndrome, affecting approximately one out of every 5,000 people, is characterized by abnormal bone growth, ectopia lentis, and aortic dilation and dissection. If left untreated, Marfan patients often die prematurely due to aortic dissection, but improved treatment dramatically decreases the death rate to near normal (Pyeritz, 2000). As Marfan patients survive and age, they will likely develop many of the vascular complications affecting the normal population, including hypertension and atherosclerosis. Therefore, it is imperative to gather biomechanical data from the Marfan vasculature so that clinicians may predict the effects of vascular complications in Marfan patients and develop appropriate methods of treatment. Although the aortas in both human patients and animal models of Marfan syndrome are stiffer than controls (Groenink et al., 1998; Jeremy et al., 1994; Marque et al., 2001), little research has been done on other arteries. This thesis compares the mechanical response of common carotid arteries from wild-type and heterozygous mgR mice, the most commonly used mouse model of Marfan syndrome. The following introductory sections briefly discuss how Marfan syndrome presents in human patients, how the extracellular matrix protein fibrillin-1 relates to Marfan syndrome, and what recently developed mouse models of the disease are currently used in the studies of the syndrome. Finally, there is a brief review of the biomechanics of the Marfan vasculature in both humans and mouse models of the disease.

This thesis follows the style and format of the Journal of Biomechanics.

Symptoms and Prognosis of Marfan Syndrome

Identified by Antonine-Bernard Marfan in 1896, Marfan syndrome is an inherited disease affecting numerous systems in the body. The disease results from a variety of mutations in the gene coding for the elastin-associated matrix protein fibrillin-1. Generally, the systems most obviously affected include the eyes, skeleton, and vasculature, although the skin, lungs, heart, muscles, and adipose tissue may be involved. The disease spans a wide variety of phenotypes, ranging from mild aortic dilation coupled with displaced lenses and slight skeletal abnormalities to death in infancy due to congestive heart failure (Pyeritz, 2000).

Marfan patients are prone to numerous skeletal malformations, including scoliosis, long bone overgrowth, arachnodactyly, and rib deformations (Pyeritz, 2000). These features were long thought to arise from decreased tension on the bones by weakened microfibrils (Keene et al., 1997), but recent studies (Neptune et al., 2003; Habashi et al., 2006) suggest that microfibrils play a role in properly presenting growth factors such as transforming growth factor β (TGFβ) to cells. TGFβ negatively affects growth and proliferation of many cells (Öklü and Hesketh, 2000), and if the mutant microfibrils fail to properly modulate TGFβ, the cartilage cells may proliferate inappropriately, laying down a scaffold for improper bone growth (Ramirez and Rifkin, 2003). Severe scoliosis is generally treated with bracing or surgical stabilization, while extreme sternum depressions may be temporarily braced and repaired after cessation of rib growth (Pyeritz, 2000).

The zonules that support the lens in the eye consist almost entirely of microfibrils (Davis et al., 2002). Marfan patients often, but not always, exhibit extreme myopia caused by elongated globes and displacement of the lens (ectopia lentis) as the result of stretched or broken zonules (Nelson and Maumenee, 1982). Sachdev et al. (2003, 2004) postulate that some fibrillin-1 mutations may render the microfibrils more susceptible to degradation by matrix metalloproteinases (MMPs) and ultraviolet light, leading to lens dislocation. If the lens displaces completely or the lens bisects the pupil, the lens is generally removed and vision is corrected with an interocular lens or with external aphakic optics (Wu-Chen et al., 2005).

While the symptoms described above may decrease a patient's quality of life, they are seldom fatal. In contrast, vascular complications of Marfan syndrome such as aortic dilation and dissection may result in early death if left untreated (Pyeritz, 2000). Bunton et al. (2001), in a review of arterial specimens from seven Marfan patients, noted unusual elastic fiber calcification, intimal hyperplasia, and collagen deposition. Although such findings are common in the elderly segment of the normal population, the average age at death of the Marfan patients studied was 33 years. Because aortic dilation may begin before birth, and progresses unpredictably, many patients are treated with β-adrenegic blocking drugs to reduce blood pressure, thus limiting the distending forces on the aorta. Doctors often advise replacing the aorta with a synthetic graft if the dilation near the aortic root advances to 50 mm in diameter. Dissections of the descending aorta generally do not proceed retrograde toward the carotids, and may be managed by reducing blood pressure and heart rate. Nevertheless, surgical repair is indicated if the

dissection approaches collateral vessels or further dissections occur (Pyeritz, 2000). With treatment, many Marfan patients have a lifespan of seventy years, which approaches that of the normal population (Milewicz et al., 2005).

Fibrillin-1, Microfibrils, and Elastic Fibers

First identified in 1986 as the gene responsible for Marfan syndrome (Sakai et al., 1986), the fibrillin-1 gene (FBN-1) is located on chromosome 15. It extends over 110 kilobases, and contains 65 exons (Kielty and Shuttleworth, 1995). The gene product, fibrillin-1, is a ~350 kDa glycoprotein containing 47 epithelial growth factor-like (EGF) and 8 TB motifs, the latter named for their homology with the latent transforming growth factor β binding proteins (LTBPs). The EGF and TB motifs contain six and eight cysteine residues, respectively, and 43 of the EGF motifs, generally noted cbEGFs, contain Ca^{2+} binding sites (Kielty et al., 2005). During the search for the FBN-1 gene, another fibrillin gene, FBN-2, was fortuitously discovered (Lee et al., 1991). The FBN-2 gene product, Fibrillin-2, is nearly identical to fibrillin-1, with the exception that a glycine-rich region replaces a proline-rich region found near the N-terminus in fibrillin-1 (Kielty and Shuttleworth, 1995). Although fibrillin-2 associates with fibrillin-1 in elastic fibers, it has a different expression pattern during development, with fibrillin-2 production generally peaking before fibrillin-1 (Zhang et al., 1994; 1995).

Fibrillin-rich microfibrils, composed primarily of fibrillins 1 and 2, are elastic proteins found in tissues throughout the body. While fibrillin microfibrils provide the sole source of elasticity in invertebrate tissues, they associate with elastin in elastic tissues such as the lungs, skin, and vasculature in vertebrates. Microfibrils also contain

numerous other accessory proteins, glycoproteins, and proteoglycans, the functions of many of which are poorly understood. Microfibril-associated glycoprotein 1 (MAGP-1) is found in nearly all microfibrils, while MAGP-2, which is structurally similar, is located only in certain tissues. Some believe MAGP-2, a cell adhesion molecule, has cell signaling effects during elastinogenesis and microfibril assembly, and that MAGP-1 plays a vital, though unknown, role in microfibrils. LTBP-1 colocalizes with microfibrils in embryonic skin and bone, while LTBP-2 colocalizes with microfibrils in elastic fibers. The proteoglycan decorin is located in the microfibrilar mantle of elastic fibers, as is the protein fibulin-2, generally at the microfibril-elastin interface (Kielty et al., 2002b). Some believe a related protein, fibulin-5, binds tropoelastin to a microfibrilar template during elastogenesis and connects elastic fibers and microfibrils to cell membranes (Ramirez et al., 2004).

Under rotary shadowing, isolated fibrillin microfibrils have an apparent diameter of ~10 nm with repeating high-mass heart-shaped structures and filamentous low-mass interbead regions. When untensioned, microfibrils have an average periodicity of ~56 nm and can elastically extend approximately forty percent (Kielty et al., 2002a). Little is definitively known about the organization of fibrillin within microfibrils, but many have proposed alignment models, including a model based on antibody binding and another based on cbEGF domain dimensions and untensioned microfibril periodicity. One such model suggests that the fibrillin molecules are arranged head to tail, and that protein folding in the proline-rich region and at certain TB-cbEGF linkages reduce the periodicity to ~56 nm. Mass-averages at various locations in the microfibril are

consistent with predicted masses if the microfibril is eight fibrillin molecules in diameter (Baldock et al., 2001).

Using molecular combing, Sherratt et al. (2003) calculated the Young's modulus of isolated microfibrils using Hooke's law. The authors justified this assumption by citing small-angle X-ray diffraction studies which indicated that microfibrils are linearly extensible in the periodicity range of 56-70 nm. As the combed length of a majority of the microfibrils was 70 nm, it seems reasonable to assume that the microfibrils were extended in their linear domain. Using two measures of microfibril diameter, transmission electron microscopy (TEM) and x-ray diffraction, they estimated the Young's modulus to be between 78 and 96 MPa. Both values are two orders of magnitude larger than the Young's modulus for single purified elastin fibers (Aaron and Gosline, 1981), and Sherratt et al. suggest that microfibrils act as stiff reinforcing filaments in elastic tissues. Interestingly, in a 1962 paper, Carton et al. found that when fresh isolated elastic fibers were extended, the force increased linearly until the fiber was extended by about 80 percent, and thereafter rose exponentially until the fiber broke at approximately 130 percent extension. The authors noted that the tested fibers did not stain for collagen, and suggest that the force-stretch behavior is intrinsic phenomenon. Aaron and Gosline (1981) suggest that each elastic fiber is encased in a collagen sheath, but given what is now known about the structure of elastic fibers, it seems reasonable to assume that the stiff microfibrils cause the behavior seen by Carton et al. If microfibrils do limit the extension of elastin, they may protect the elastin from long-term damage,

playing a role in tissue homeostasis as suggested in Charbonneau et al. (2004), Ramierez and Pereira (1999), and Arteaga-Solis et al. (2000).

Davis et al. (2002) suggest that commonly used tissue and microfibril preparation methods remove microfibril accessory proteins. Using a quick-freeze technique, they found that the microfibrils contained three small beads between two larger beads located ~50 nm apart, which they believe represent the beads seen in previous studies of isolated microfibrils such as those conducted by Kielty et al. (2002a). The large beads were aligned between microfibrils, with MAGP-1 staining fibers extending between the larger beads. Disruptive treatment of the zonules before imaging produced isolated microfibrils with a similar appearance to those found in previous studies, and small monomer beads with numerous thin fibers attached. Davis et al. believe the small beads in the interbead region consist of accessory proteins which were removed during preparation in previous studies, and that believe the separated beads represent aggregates of MAGP-1 or other auxiliary proteins.

In a study of cultured pigmented epithelium (PE) cells, which produce microfibril networks but do not secrete elastin, Robb et al. (1999) found two populations of microfibrils, one coated with an unknown material and one that was uncoated. Although the coating material was not identified, the coated microfibrils appeared similar to sub-endothelial microfibrils found in the aorta, which stained strongly for fibronectin in previous studies (Davis, 1993; 1994). When the PE cells were transfected with genes coding for bovine tropoelastin, they produced a microfibril-elastin matrix similar to cultured controls, with the elastin preferentially located near coated

microfibrils. However, the elastin fibers were not surrounded by a microfibrilar sheath, as seen in elastic tissues, which the authors attribute to lack of an appropriate structural and mechanical environment (Robb et al., 1999).

Although tropoelastin can self-assemble, or coacervate, *in vitro* without association with microfibrils (Bellingham et al., 2001), Kozel et al. (2003) argue that initial deposition of elastin does not involve coacervation, but instead suggest that microfibrils nucleate elastin aggregates. Given this theory, one would expect that a lack of fibrillin-1 would prevent elastogenesis. A recent study (Carta et al., 2006) found that mice without the fibrillin-1 gene form intact elastic fibers, although these mice usually died within two weeks, primarily due to aortic rupture. At death, the mice had disorganized elastic lamina, but normal elastin cross-linking, proving that fibrillin-1 is not necessary for deposition and cross-linking of elastin. Although mice without the fibrillin-2 gene have a normal lifespan, fibrillin-2 null mice crossed with heterozygous or homozygous fibrillin-1 null mice have a significantly decreased survival rate, often dying shortly after embryonic day 14.5. Analysis of embryonic day 14.5 double null mice showed decreased or delayed elastogenesis, indicating that elastin deposition requires fibrillin microfibrils. Carta et al. believe that fibrillin-1 controls neonatal maturation of the elastic lamina and structurally supports the aortic wall, while fibrillin-2 acts as a scaffold for elastin deposition, although fibrillin-1 can compensate for a lack of fibrillin-2.

Given the large number of calcium-binding motifs in the fibrillin molecule, one would expect that metal ions would play a significant role in both the molecule and its

aggregates. In their study of cultured microfibrils, Cardy and Handford (1998) examined the effect of metal ions on the periodicity and flexibility of individual microfibrils. Using microfibrils produced by cultured fibroblasts, they found that calcium chelation by both EGTA and EDTA reduced the periodicity and increased the flexibility of the microfibrils. This effect was reversible when the microfibrils were placed in a high Ca^{2+} solution, but were not reversible in a high Mg^{2+} solution. Earlier studies by the same group on cultured normal and Marfan microfibrils demonstrated the effect of a single mutation in an interbead calcium-binding EGF. The researchers synthesized both a normal and a mutant peptide, duplicating a specific cb-EGF sequence known to cause Marfan syndrome. When subjected to nuclear magnetic resonance analysis, the mutant peptide showed a slight difference from the normal, and the difference increased markedly when both peptides where saturated with Ca^{2+}. Ultrastructural studies of intact mutant microfibrils further illustrated the effects of the mutation, with the interbead region of the mutant fibrillin appearing diffuse and similar to microfibrils treated with EDTA, even with the application of calcium ions (Handford et al., 1995).

Although elastin is known to have a half-life of approximately 70 years (Kielty et al., 2005), the half-life of fibrillin microfibrils has not been quantified. However, it is theorized that both elastic fibers and microfibrils have a half-life similar to that of elastin (Kielty and Shuttleworth, 1995). Ross and Bornstein, in their 1969 paper, showed that both elastin and microfibrils were generally unaffected by collagenase and hyaluronidase, but that microfibrils were degraded by trypsin or chymotrypsin while the elastin remained intact. When the elastic fibers were treated with elastase, the

microfibrils were initially unaffected, but partial degradation was apparent after 45 minutes of exposure.

In their investigation of the protective effects of Ca^{2+} binding against proteolysis, Reinhardt et al. (1997) studied whole fibrillin-1 molecules and recombinant fibrillin fragments. The fragments, in addition to the complete fibrillin molecule, showed much higher rates of degradation in the presence of EDTA than Ca^{2+} when exposed to several proteinases, including trypsin and elastase. The fragments were significantly degraded after one hour of incubation with each enzyme and EDTA, while incubation with the same enzymes and Ca^{2+} had very little effect. The protective effect of calcium ions was not complete, as the fragments were unable to withstand 23 hours of incubation. The digestion products indicated that removal of calcium from the individual cb-EGF motifs caused a structural change, rendering the fibrillin fragments (and, by extension, the fibrillin molecule) susceptible to proteolysis. Not all of the digestion products can be explained by this theory, however, and it was proposed that calcium binding stabilizes tandem arrays of cb-EGF motifs in an as yet unknown way.

Mouse Models of Marfan Syndrome

In order to study Marfan syndrome in a laboratory setting, Ramirez et al. developed two strains of mice that display many of the phenotypic marks of the disease, including aortic dissections. One strain, mgΔ, produces abnormally short fibrillin-1 at levels significantly less than normal. The knockouts for this strain appear phenotypically normal at birth, but die within two weeks due to dissection of the ascending aorta (Ramirez and Pereira, 1999). The second strain, mgR, was discovered fortuitously

during the development of mgΔ and produces normal fibrillin at levels a fifth that of normal (Pereira et al., 1999).

Mice homozygous for the mgR mutation have apparently normal vascular elastic lamina at birth, but develop obvious focal calcifications of the elastic lamina as early as 6 weeks. At approximately 8 weeks, medial monocyte infiltratation develops, in addition to fragmented elastic lamina, loss of elastin, and aortic dilation. After 9 weeks, intimal hyperplasias appear near the calcified lesions, as well as smooth muscle cell (SMC) invasion and disorganized deposition of elastin and collagen. The mgR strain died at an average age of 3.6 months, often with signs of vascular involvement (Pereira et al., 1999). Studies by Bunton et al. (2001) on the mgR strain found elastic lamina breakdown within the media while the internal and external elastic media remained intact. They also noted an increased synthetic phenotype among the SMCs, inflammatory cell infiltration, and increased MMP levels. The researchers suggested further that mgR mice lacked microfibrils due to decreased production of fibrillin-1, and that this deficiency reduced the number of connections between the smooth muscle cells and the elastic lamina. As the mice aged, the cumulative effect of normal blood pressure broke the connections further, removing the SMCs from their normal environment within the extracellular matrix. This loss of context caused the SMC phenotype to become synthetic, producing matrix components as well as MMP9, inducing early elastolysis as the cells attempted to return their external environment to normal. As the disease progressed, the external and internal lamina were disrupted, allowing

inflammatory cells to migrate in, which in turn caused extensive elastolysis and wall breakdown.

Fibrillin and Vascular Mechanics

Due to the devastating effects of aortic dilation and dissection, the aorta in Marfan syndrome has been studied extensively in an attempt to predict and treat progressive aortic dilation. Jeremy et al. (1994) reported that echocardiographic measurements of vascular mechanics, such as pulse wave velocity and aortic distensibility, indicated that Marfan ascending aortas were substantially stiffer than those of age-matched controls. Although it is well-known that that aorta stiffens with age (Avolio et al., 1983; 1985), this 1994 study found that the stiffness of Marfan aortas was greater at all ages than that of the oldest controls. The slope of the aortic-stiffness/age relation was also increased in the Marfan group, which the authors believe indicates an altered load-bearing capacity due to progressive elastin deterioration within the vessel wall. Using magnetic resonance imaging, Groenink et al. (2001) measured increased pulse wave velocities along the entire length of the aorta in Marfan patients as compared to healthy controls, as well as decreased distensibilities in the aortic arch and near the aortic bifurcation. These data indicate that the entire aorta stiffens in Marfan syndrome, not only the aortic root or arch.

Using pulse wave velocity measurements, Marque et al. (2001) calculated a four-fold increase in the elastic modulus of homozygous mgR aortas as compared to wild-type mice. They also measured the pulse wave velocity at different pressures by inducing hypotension using sodium nitroprusside. The pulse wave velocity verses

pressure curves had similar low-pressure values for both the knockout and wild-type mice, but the knockout curve increased nearly twofold compared to the wild-type curve at normal pressures. Groenink et al. (1998) addressed the effects of pharmacological pressure reduction on pulse wave velocities. Application of a β-blockade increased the distensibility throughout the aorta, but did not produce a statistically significant difference in aortas of control patients. Except at the level of the aortic root, distensibility between the Marfan and control groups were not statistically different either before or after β-blockade. The pulse wave velocity did decrease significantly after medication in the Marfan group, and although the pulse wave velocities between the two groups were statistically different before the β-blockade, they were not afterward. The authors believe that decreasing blood pressure in Marfan patients results in increased compliance because mechanical behavior of the vessels is dominated by collagen, which has an exponential stress-strain response function. Thus, a blood pressure decrease in Marfan patients would have a greater effect on distensibility than in control patients, whose aortas have a more linear stress-strain response due to the presence of intact elastic lamina in the media.

Although mutated fibrillin has a dramatic effect on vascular mechanics, several studies have linked normal fibrillin-1 genotypes to altered pulse pressure, an indirect measure of vascular stiffness. Briefly, the differences between fibrillin-1 genotypes are based on analysis of a non-coding region, intron 28, within the fibrillin gene containing a variable number of tandem repeats, and thus a different length in basepairs. Although four different repeat lengths have been identified within intron 28, only three of the

sixteen possible pairings are commonly found in both healthy patients and those with abdominal aortic aneurysm (AAA) or coronary artery disease (CAD). Powell et al. (1997) suggested that in healthy patients, the three genotypes, 2-2, 2-3, and 2-4, strongly correlate to differences in pulse pressure, with less strong correlations to differences in mean pulse pressure and mean systolic pressure. Specifically, the 2-3 group had higher pulse pressures, the 2-4 group had lower pulse pressures, and the 2-2 group had pulse pressures around the median. These findings confirmed a previous study of patients with AAAs. In addition, the previous study found that patients with the 2-3 geneotype were more likely to have popliteal aneurysms in addition to the AAA, while the 2-4 group did not have popliteal aneurysms. Both groups with and without popliteal aneurysms had similar incidences of the 2-2 genotype and rarer genotypes (MacSweeney et al., 1996). A study of patients with coronary artery disease (CAD) found that the 2-3 genotype correlated strongly to an increased vascular impedance and the severity of the disease, measured in terms of repeat angioplasties and a maximum occlusion of more than 90 percent. In addition, 14 percent of the CAD patients had a rare genotype compared to 5 percent found in the healthy population of the 1997 study (Medley et al., 2002). A recent study by Powell et al. (2005) correlated to an increase in aortic stiffness, mean arterial pressure, and pressure strain elastic modulus in healthy, middle-aged patients with the 2-3 geneotype. These findings suggest that even differences in normal fibrillin-1 play a role in the mechanics of the vasculature, possibly by subtly altering the arterial wall structure.

In summary, mice homozygous for the mgR mutation have abnormalities in their vasculature and serve as a disease model for the human disease of Marfan syndrome. It is thus constructive to study these mice to provide clinicians with data to effectively treat Marfan patients. However, the similarity of the Marfan vasculature to that of the vasculature in advanced age expands the impact of Marfan studies to the general population. In addition, fibrillin-1 is thought to present the growth factor TGF-β to cells, making mgR mice applicable to the study of cell signaling in development and maturity. It is by studying both the mechanics and biological response that we can begin to model the vasculature in both health and disease, allowing clinicians to appropriately predict and treat issues that arise in diseases such as Marfan syndrome, as well as problems developed in the normal aging process.

BIOMECHANICAL TESTING

In order to further understanding of the Marfan vasculature, we wish to study the properties of carotids from a mouse model of Marfan syndrome. To this end, the specific goals of this project are:

(1) To quantify the response of wild-type and heterozygous mgR mouse carotid arteries to applied loads considering:
   (a) Responses with (active) and without (passive) SMC basal tone,
   (b) Axial and circumferential directions.

(2) To evaluate differences between wild-type and heterozygous arteries.

(3) To compare the wild-type and heterozygous responses to available data for mice heterozygous for elastin and mouse models of muscular dystrophy.

(4) To determine the utility of heterozygous carotids as a model of the Marfan vasculature.

This following sections describe the experimental set-up, relate the results of the experimental procedures, and examine the findings in a physical and historical context.

Materials and Methods

Artery Isolation and Setup in Computer Controlled Testing Device

Breeding pairs of mgR+/- mice were given by Dr. Francesco Ramirez (University of Medicine and Dentistry of New Jersey), and their offspring used for experiments. All animals were maintained by the Texas A&M University Comparative Medicine Program (CMP) and were used in accordance with the University Laboratory

Animal Care Committee (ULACC) guidelines. MgR+/- (n = 6) male C57BL/6J-129Sv mice and their wild-type male littermates (n = 6), between 8 and 14 weeks old, were euthanized with a lethal injection of sodium pentobarbital (~50mg/kg IP) and the left and right common carotid arteries were isolated. One artery, generally the left, was placed in warm advanced Dulbecco's modified Eagle's medium (ADMEM, Invitrogen, Inc.), supplemented with 2% heat-inactivated fetal bovine serum (HI-FBS, Atlas Biologicals), 10 mL 200 mM L-glutamine, as well as 1000 units/L penicillin and 1000 g/L streptomycin (P/S, Invitrogen, Inc.), and mounted on glass perfusion cannulae at both extremities using 6-0 suture.

The cannulated arteries were placed in a bath of fresh, warm ADMEM supplemented as above within the incubator chamber of the testing device. Flow was initiated adventitially from reservoirs of supplemented ADMEM and a load cell was attached to the distal cannula. Once an image was obtained, measurements in the unloaded configuration (with mean pressure P = 0 mmHg and axial load f = 0 g) were measured. The unloaded diameter D was noted and unloaded axial length where the vessel just begins to bend was measured as described by Gleason et al. (2004a). After recording the unloaded length, the vessel was stretched to an axial stretch (λ_z) of 1.5, pressurized to 80 mmHg, and intraluminal flow was initiated (Q = 0.5 ml/min). This condition was maintained for approximately fifteen minutes, until all bubbles exited the tubing. After this equilibration period, intraluminal flow was stopped and the vessel was preconditioned for two cycles by axially stretching the vessel to 1.8 and cycling the pressure from 0 to 160 mmHg. After preconditioning, the unloaded length and diameter

were measured and recorded again, and the inner and outer diameters were measured by manually adjusting video-calipers in the following configurations: P = 0 mmHg and λ_z = 1.2, 1.4, 1.6, and 1.8; P = 40 mmHg and λ_z = 1.4, 1.6, and 1.8; P = 80 mmHg and λ_z = 1.6 and 1.8; and P = 100 mmHg and λ_z = 1.8.

Mechanical and Functional Testing

Mechanical testing consisted of two parts, pressure diameter (*P-D*) and force-stretch (f-λ_z) tests. During the *P-D* test, the vessel was axially stretched to 1.65, 1.75, and 1.85 and held at that stretch while P cycled from 0 to 160 mmHg twice, resulting in one preconditioning curve and one curve used as experimental data per stretch. Similarly, during the f-λ_z tests, the pressure was maintained at 0, 60, 100, and 160 mmHg while λ_z was decreased until the vessel bent. For each pressure, the vessel was then stretched until the axial force exceeded 0.9 g and then returned to an unloaded length twice.

After mechanical testing, the vessel was stretched to λ_z = 1.65 and pressurized to P = 80 mmHg for fifteen minutes to equilibrate for the function test. At the end of this period, the adventitial flow was stopped and 150 μL of 10^{-3} M phenylephrine (PE), which tests the contractile ability of smooth muscle cells, was added to the ~15 mL bath for a final concentration of ~10^{-5}. After fifteen minutes, 150 μL of 10^{-3} M carbamylcholine chloride (CCh), which tests the endothelium-dependent smooth muscle cell relaxation, was added. After fifteen minutes later, 150 μL of 10^{-2} M sodium nitroprusside (SNP), which induces endothelium-independent smooth muscle cell relaxation, was added, and the vessel was allowed to equilibrate for fifteen minutes.

After functional testing, three vessels from each group were mechanically tested under passive conditions. The bath was emptied, rinsed twice with warm Hank's Balanced Salt Soultion (HBSS, Invitrogen, Inc.) without calcium or magnesium, and refilled with warm calcium-free HBSS to which 150 μL of 10^{-2} SNP was added. The vessel was allowed to equilibrate at P = 80 mmHg and λ_z = 1.65 for ten minutes, and then the vessel was mechanically tested as described above.

Post Processing

The passively tested vessels were unloaded, removed from the device, and fixed in 4% paraformaldehyde for one hour. Afterwards, the arteries were immersed in a cryoprotectant (30% sucrose) overnight. The vessels were then mounted in OCT medium (Tissue Tek) in isopentane cooled with liquid nitrogen, and stored at -80^{o}C for future sectioning and immunohistochemical analysis. The untested carotids from each mouse and the non-passively tested vessels were flash frozen in liquid nitrogen and stored at -80^{o}C for future isolation and analysis of RNA and protein.

Data Processing

Functional vessels were selected for analysis as quantified by at least 30 percent contraction in response to PE (as compared to the final diameter of the vessel fifteen minutes after application of SNP) and at least 10 percent dilation (from the contraction caused by PE) in response to CCh. Axial force, axial stretch, pressure, and outer diameter data were collected for each vessel at 4 Hz during all tests. The inner and outer diameters measured allowed us to calculate the volume of the vessel wall using

$$V = \pi \, l \left(b^2 + a^2 \right) \qquad (1)$$

where l is the length, a is the inner radius, and b is the outer radius in the current configuration. The four different volume values found at P = 0 mmHg were averaged to give $\overline{V}$. The remaining six volume calculations were used to test the accuracy of the calculated inner radius based on the volume estimate. Assuming incompressibility, the mean volume and outer diameter values allowed the luminal radius a and the wall thickness h to be computed at all states using the following formulae:

$$a = \sqrt{b^2 - \overline{V}/(\pi l)}, \tag{2}$$

and

$$h = (b - a). \tag{3}$$

This, in turn, allowed us to calculate the mean axial and circumferential Cauchy stresses (σ_z and σ_θ, respectively) at every test point using

$$\sigma_z = \frac{f}{\pi\left(b^2 - a^2\right)}, \tag{4}$$

and

$$\sigma_\theta = \frac{Pa}{h}. \tag{5}$$

The axial stretch ratio was calculated via

$$\lambda_z = l/L \tag{6}$$

where L is the unloaded length, whereas the circumferential stretch ratio was calculated using the inner radii

$$\lambda_\theta = a/A \tag{7}$$

where *A* is the inner radius calculated using the unloaded length and unloaded outer radius. The inner and outer radii, wall thickness, axial and circumferential stresses and stretches can thus be calculated at every test-point using the unloaded configuration measured prior to testing. After interpolating between test-points, the loaded dimensions, axial force, and axial and circumferential stresses were analyzed with SPSS software using one-factor analysis of variance (ANOVA) for $p<0.05$. The body weights and ages of the mice, as well as the mean wall volumes and unloaded arterial dimensions were similarly analyzed for $p<0.05$. For the *P-D* test, the outer diameter and axial force were compared between pressures of 2 and 160 mmHg, and the circumferential stress was compared for circumferential stretches between 0.28 and 3.8 (these ranges of independent variables were common for all vessels of the two genotypes, thus enabling statistical comparison). For the *f*- λ_z test, axial force and axial stress were compared for axial stretches between 0.5 and 2.5.

Another comparison from the *f*- λ_z test was made. It is known that blood vessels are extended far beyond their unloaded length *in vivo*, and that at the *in vivo* axial stretch ($\lambda_{z\ in\ vivo}$, the *in vivo* length normalized by the unloaded length), the axial force tends to remain constant over a range of pressures (Humphrey, 2002). One way to discern the *in vivo* axial stretch of arteries already isolated from animals is to examine the results of the force-stretch curves and find the point where the force is the same for different pressures (in this case, pressures of 60, 100, and 160 mmHg). The axial stretch corresponding to this common axial force represents the *in vivo* axial stretch, where the axial force remains relatively constant as the pressure is cycled. The intersection points of the 60,

100, and 160 mmHg force-stretch curves were found for each artery (by interpolating between the two closest axial stretch points) and the three intersection points were averaged to yield an estimate for that vessel's *in vivo* axial stretch. The $\lambda_{z\ in\ vivo}$ values were compared using ANOVA for $p<0.05$.

The outer diameters measured in response to the various agonists during the function test were normalized to the final diameter in the presence of SNP and compared using ANOVA for $p<0.05$.

Results

Mouse Characteristics and Functional Response

The mean mouse characteristics and vessel properties are shown in table 1. With the exception of the unloaded outer diameter, OD, no values were significantly different between the wild-type and heterozygous groups. Basal tone, contraction to PE, and dilation to CCh are normalized to the final diameter after fifteen minutes in the presence of SNP. Wild-type and heterozygous groups had an average basal tone of 97 and 94 percent, respectively, but in the vessels passively tested, the vessels dilated further, resulting in a average basal tone of approximately 90 percent of the final diameter in HBSS without Ca^{2+}. Representative function curves can be seen in figure 1. The wild-type mouse was tested on 6/16/06 and had a basal tone of approximately one percent, while the heterozygous mouse was tested on 6/23/06 and had a basal tone of approximately 10 percent. When compared to previous studies on different strains (C57BL/6 and FVB/N), the endothelial dilation was quicker and not as long-lasting, with the vessel dilating to its maximum CCh diameter within three minutes and then

decreasing to a level slightly above its minimum diameter in the presence of PE alone. C57BL/6 vessels reached their maximum diameter shortly before SNP was added, and FVB/N vessels reached their maximum diameter at about ten minutes and then decreased to a level below the minimal diameter in the presence of PE alone (Dye, 2005; Gleason et al., 2004a).

Mechanical Response—Pressure Diameter Tests

The general mechanical response of both groups of mouse carotid arteries to biaxial testing was similar to that reported for other mouse carotids tested in our lab (Dye, 2005; Gleason et al., 2004a) and elsewhere (Wagenseil et al., 2005). During the pressure-diameter tests, as the pressure increased, the vessel was initially rather compliant, with the diameter increasing rapidly. However, at near-physiological pressures (80-100 mmHg) the vessel became less compliant and the diameter increased only slightly. Figures 2 and 3 show the averaged wild-type and heterozygous pressure-diameter curves, with basal tone and in the passive state, respectively. The curves separate move downward (i.e. become less complaint) as the axial stretch increases, especially at higher pressures. Although the active wild-type PD curves were not generally significantly different when compared to active heterozygous curves, the differences between the active PD curves at $\lambda_z = 1.65$ did reach statistical significance at some sub-physiological pressures, namely 2-6, 28, 32-60, 64-66, and 70-72 mmHg. One point, 4 mmHg, was statistically different in the active PD curves at $\lambda_z = 1.75$. The passive PD curves did not show a statistical difference when the wild-type and heterozygous data were compared, possibly due to low sample sizes.

Table 1
Comparisons of mouse and vessel properties for wild-type and heterozygous mgR mice.

	Wild-Type	**Heterozygous**
	Animal Properties	
Body Weight (g)	21.800 ± 1.479	23.283 ± 1.902
Age (wks)	11.235 ± 1.876	11.305 ± 1.060
	Vessel Properties	
V (mm^3)	0.187 ± 0.021	0.193 ± 0.040
$\lambda_{z\ in\ vivo}$	1.706 ± 0.077	1.704 ± 0.062
***f* at $\lambda_{z\ in\ vivo}$ (mN)**	3.301 ± 0.693	3.200 ± 0.558
	Unloaded Dimensions	
L (mm)	3.093 ± 0.372	3.542 ± 0.815
OD (μm)	363 ± 21	342 ± 17*
A (μm)	116 ± 15	108 ± 13
H (μm)	65.0 ± 4.5	63.0 ± 5.5
	Functional Response	
Basal Tone	0.972 ± 0.027	0.940 ± 0.057
Contraction to PE	0.637 ± 0.046	0.669 ± 0.025
Dilation to CCh	0.783 ± 0.064	0.820 ± 0.023
OD with SNP (μm)	541 ± 26	532 ± 14

All data are represented as mean ± standard deviation. A * indicates statistical significance when a heterozygous value is compared to the wild-type ($p<0.05$).

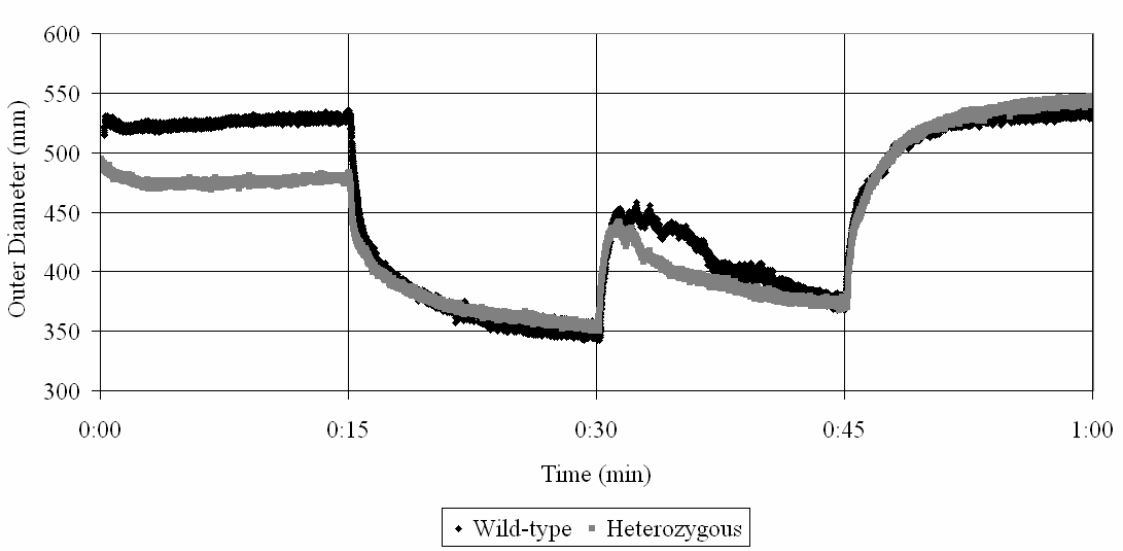

Fig. 1. Representative functional response curves. PE was added at 15 minutes, CCh at 30 minutes, and SNP at 45 minutes.

Figures 4 and 5 show representative active and passive circumferential stress-strain curves. The wild-type vessel was tested on 6/14/06 and the heterozygous vessel was tested on 7/24/06; these data were chosen because their *in vivo* stretches (as calculated from the force-stretch tests under basal tone) are similar to the average *in vivo* stretches with basal tone. Overall, the wild-type and heterozygous circumferential stress-strain values were not significantly different, either with or without basal tone. The active heterozygous curves seem to increase in variability as the axial stretch increases, and the curves shown are similar to the majority of data collected. The passive heterozygous curves shown grow closer to the mean as the axial stretch increases, and represent the left-most curves of the set. Both the active and passive wild-type data seem to decrease in variability as the axial stretch increases, and the wild-type data curves shown are to the right of the mean. No statistically significant difference was found between either the active wild-type and heterozygous curves or the passive wild-type and heterozygous curves. In both active and passive tests for both groups, the vessels exhibit stress stiffening as the axial stretch increases, moving to the left on the circumferential stretch axis.

Because the axial force remains constant over a range of pressures at the *in vivo* axial stretch (Humphrey, 2002), force-pressure curves can confirm the *in vivo* stretches calculated from the force-stretch tests. Figures 6 and 7 show the averaged active and passive force-pressure curves, respectively. In both figures, the force decreases at an axial stretch of 1.65 and increases at an axial stretch of 1.75, indicating that the *in vivo*

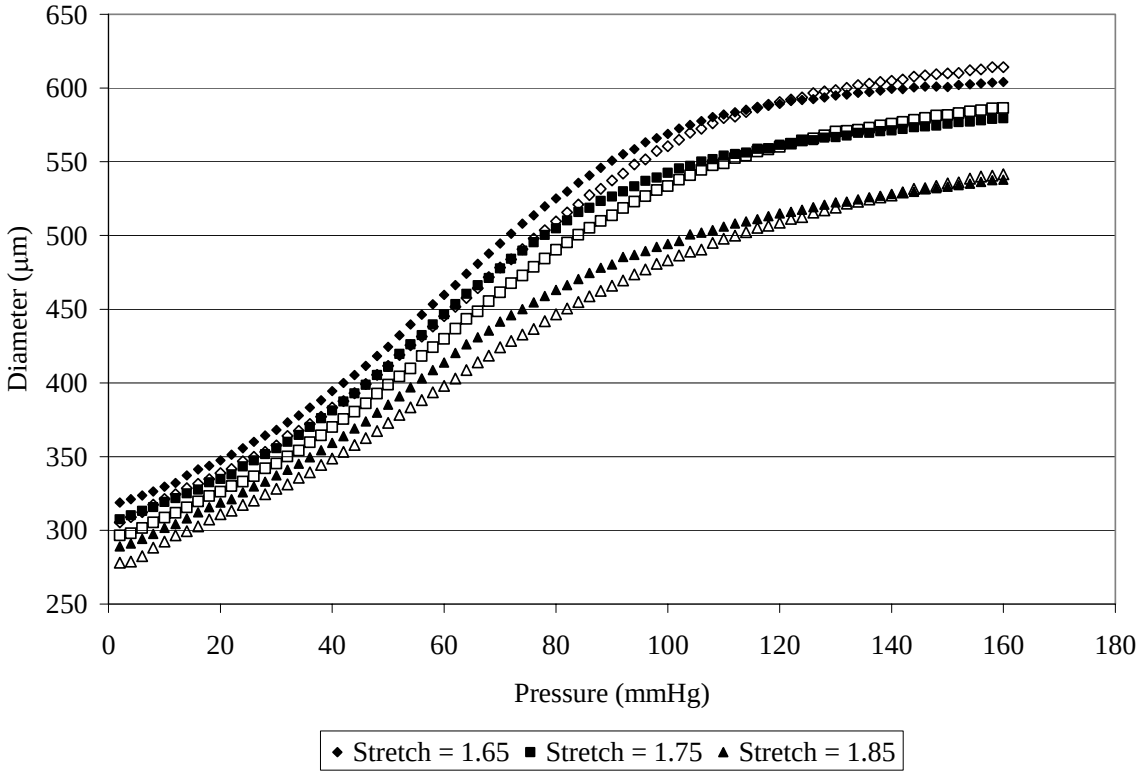

Fig. 2. Averaged active wild-type and heterozygous pressure-diameter curves. Wild-type curves are denoted by solid symbols, heterozygous curves by hollow symbols.

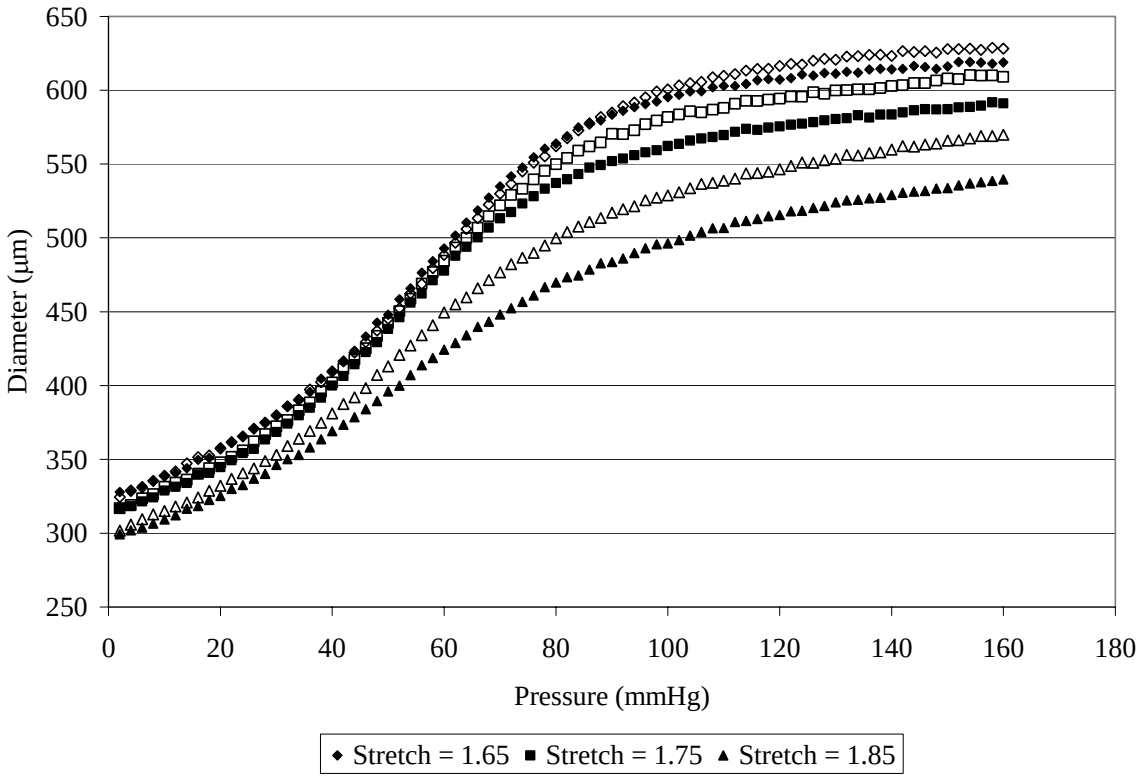

Fig. 3. Averaged passive wild-type and heterozygous pressure-diameter curves. Wild-type curves are denoted by solid symbols, heterozygous curves by hollow symbols.

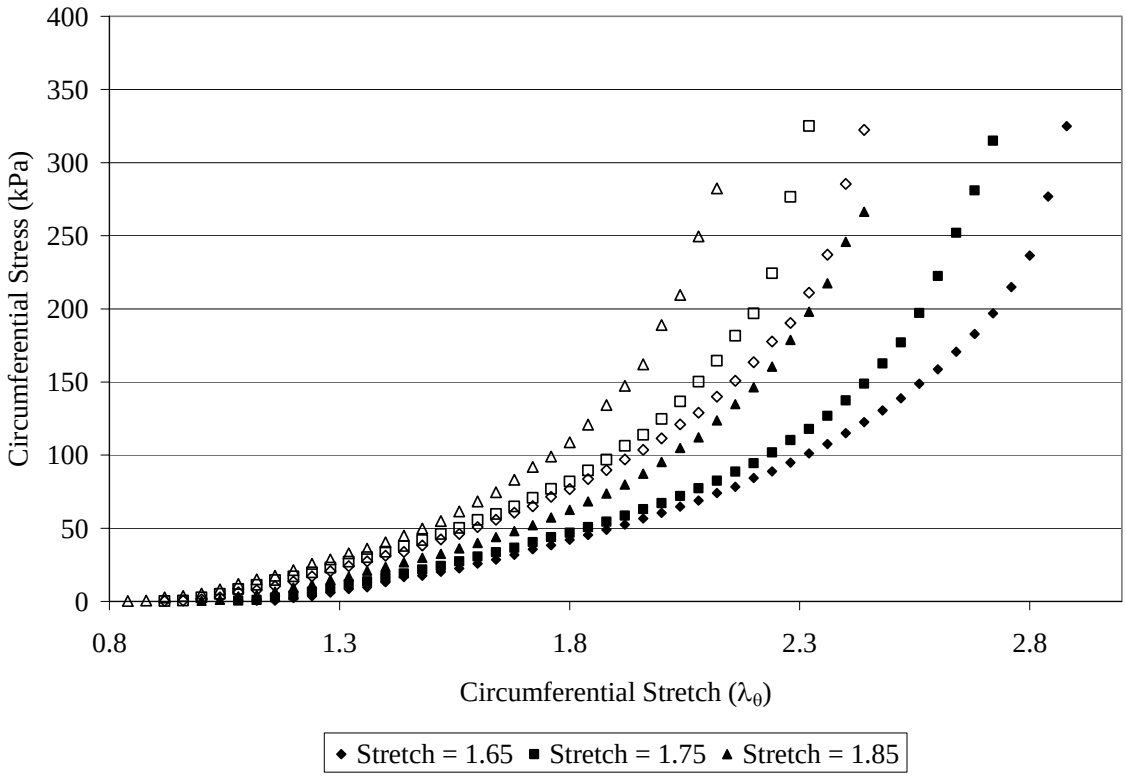

Fig. 4. Representative active wild-type and heterozygous circumferential stress-strain curves. Wild-type curves are denoted by solid symbols, heterozygous curves by hollow symbols.

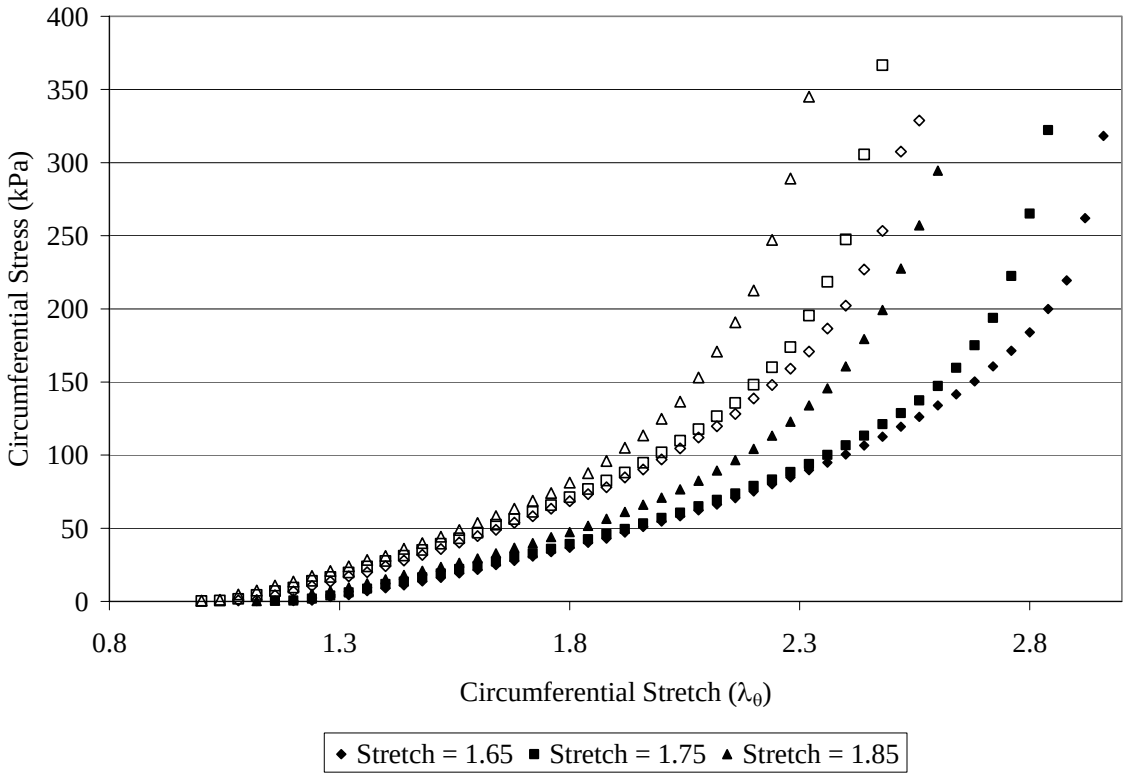

Fig. 5. Representative passive wild-type and heterozygous circumferential stress-strain curves. Wild-type curves are denoted by solid symbols, heterozygous curves by hollow symbols.

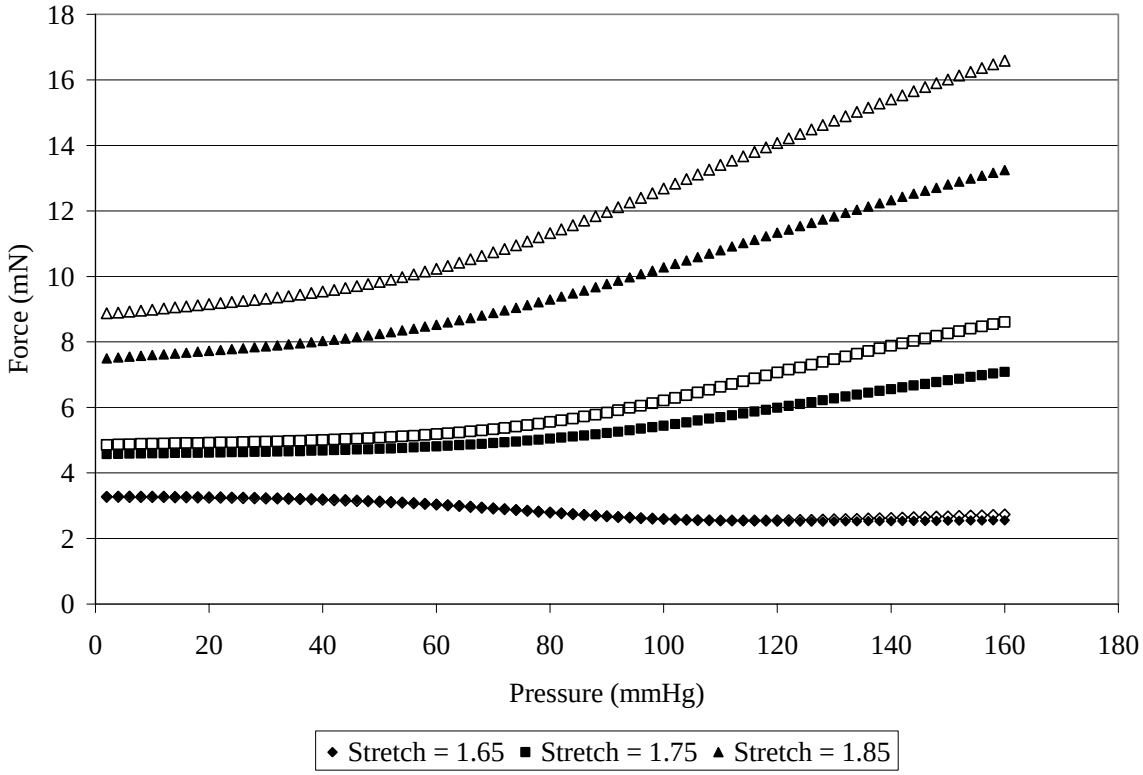

Fig. 6. Averaged active wild-type and heterozygous force-pressure curves. Wild-type curves are denoted by solid symbols, heterozygous curves by hollow symbols.

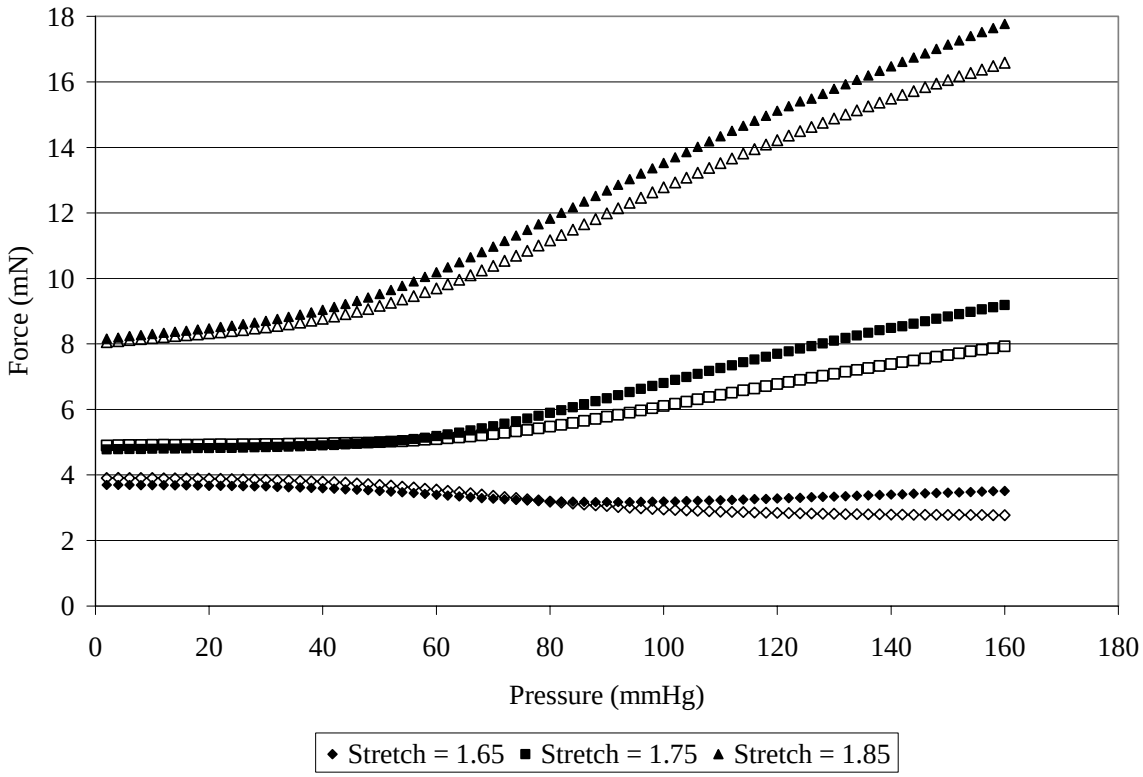

Fig. 7. Averaged passive wild-type and heterozygous force-pressure curves. Wild-type curves are denoted by solid symbols, heterozygous curves by hollow symbols.

axial stretch lies somewhere between 1.65 and 1.75. No statistical difference between the wild-type and heterozygous curves was found, either in the active or passive case.

Mechanical Response—Load-Stretch Tests

Figures 8 and 9 show the intersections of representative active wild-type and heterozygous force-stretch curves, respectively. The wild-type vessel was tested on 6/14/06 and the heterozygous vessel was tested on 7/24/06. The 60, 100, and 160 mmHg curves in both the wild-type and heterozygous vessel intersect at an axial stretch of approximately 1.70, with an axial force of 3 and 3.5 mN, respectively. Passive curves are similar, and are shown with their active counterparts in Appendix A. Figures 10 and 11 show the axial stress-stretch curves for the representative active wild-type and heterozygous vessels. The maximum axial stress is less than the maximum circumferential stress shown in Figures 4 and 5. In both the axial force-stretch and axial stress-stretch graphs, the x-intercepts of the curves move to the right and the slope increases as the pressure increases. Overall, the wild-type axial force-stretch and axial stress-stretch values were not significantly different from the heterozygous values.

Figure 12 and table 2 show the averaged *in vivo* stretches and forces for wild-type and heterozygous vessels in both the active and passive state. No statistically significant difference was found between the active wild-type and heterozygous data or between the passive wild-type and heterozygous data. Although the *in vivo* stretch decreased slightly under passive conditions, the change was not significant when the active and passive groups were compared by genotype. Similarly, the passive *in vivo* forces were not significantly different from active *in vivo* forces.

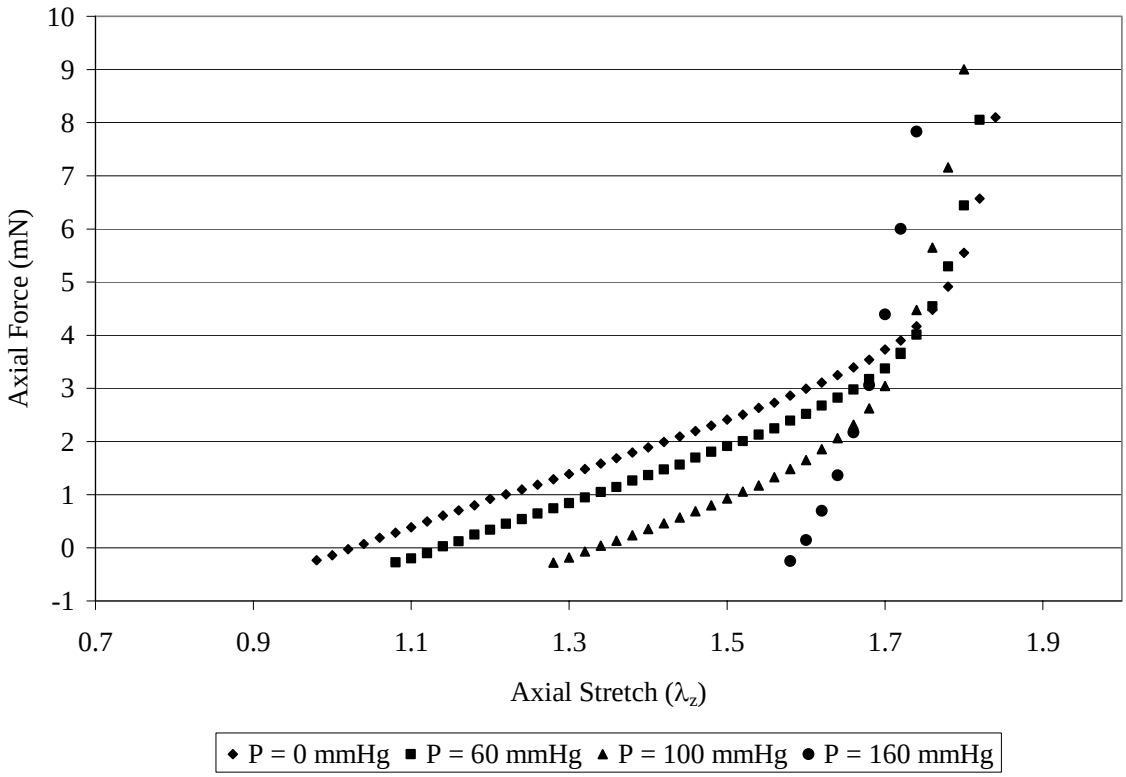

Fig. 8. Representative active wild-type axial force-stretch curves.

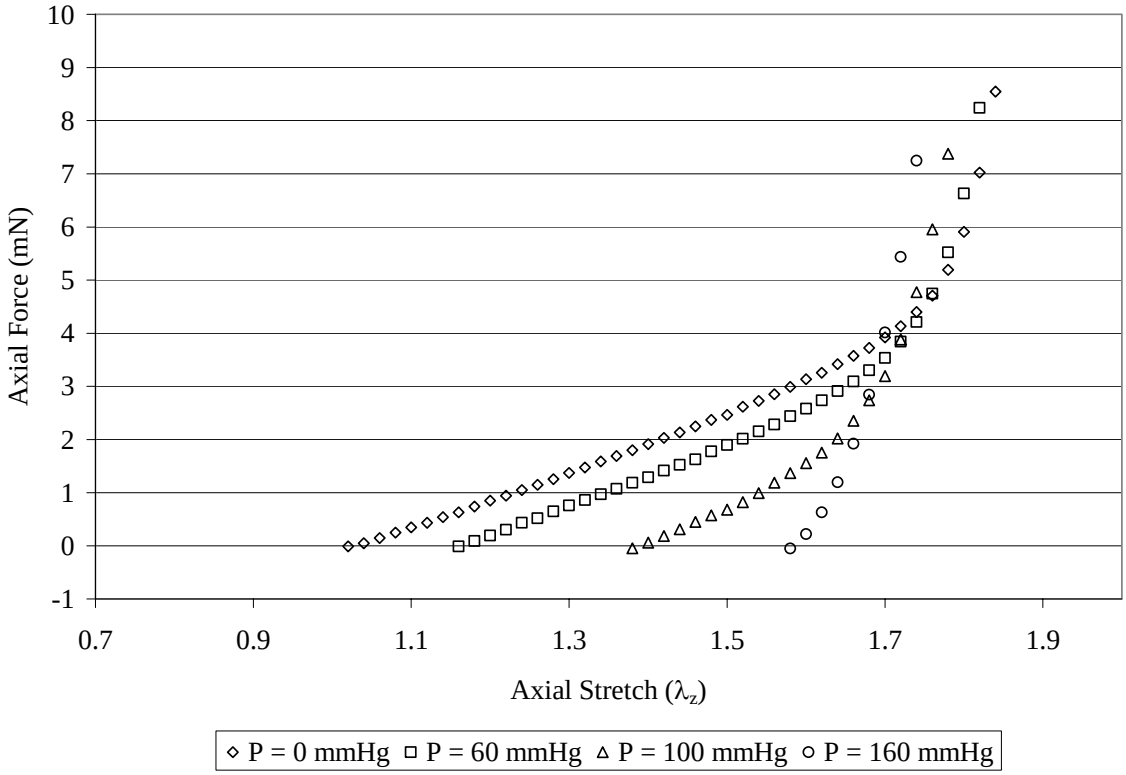

Fig. 9. Representative active heterozygous axial force-stretch curves.

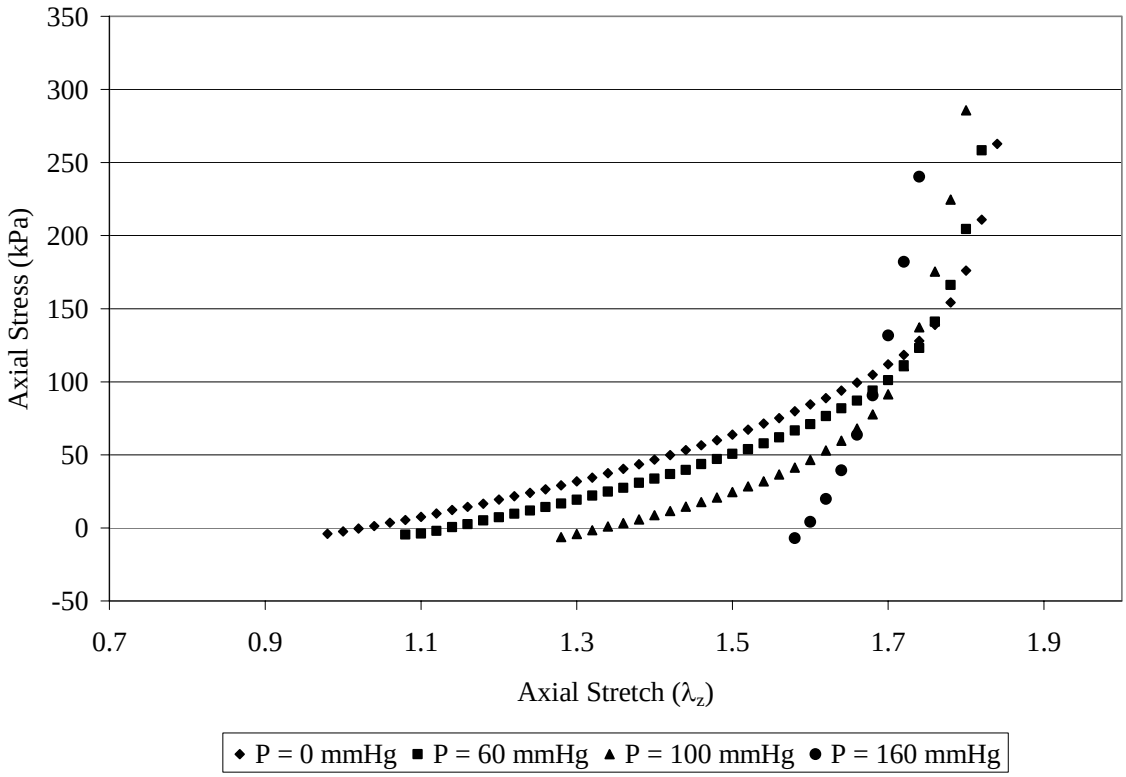

Fig. 10. Representative active wild-type axial stress-stretch curves.

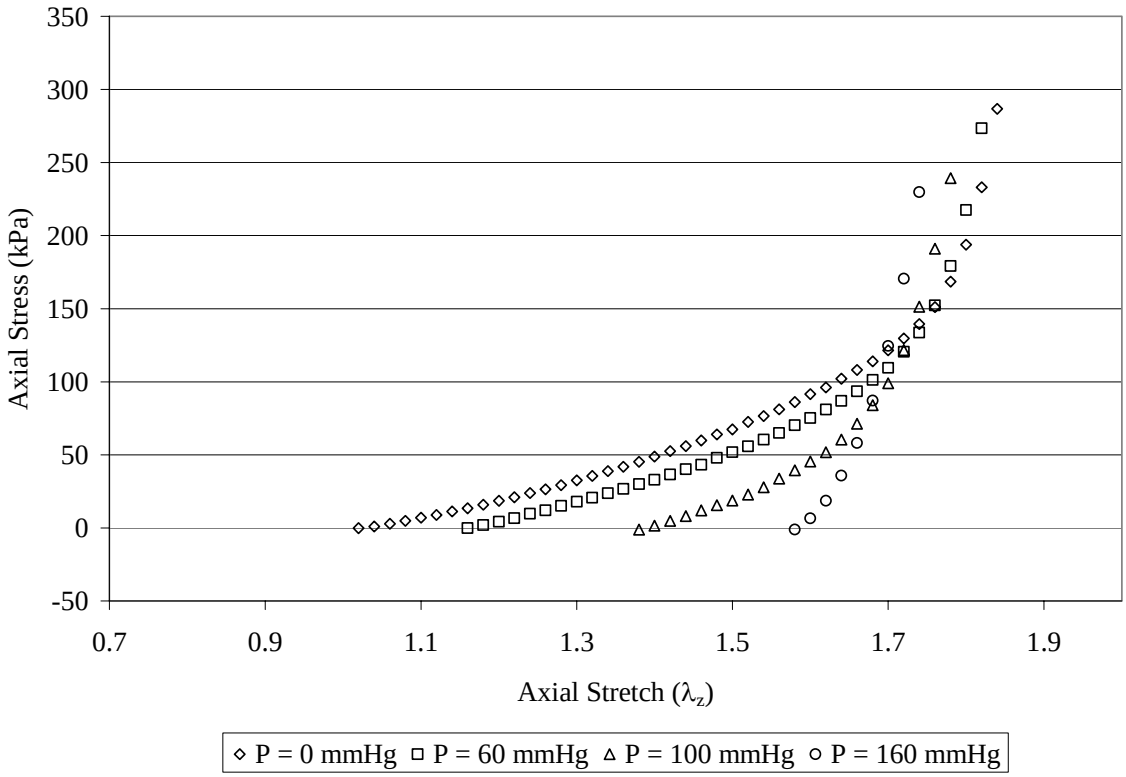

Fig. 11. Representative active heterozygous axial stress-stretch curves.

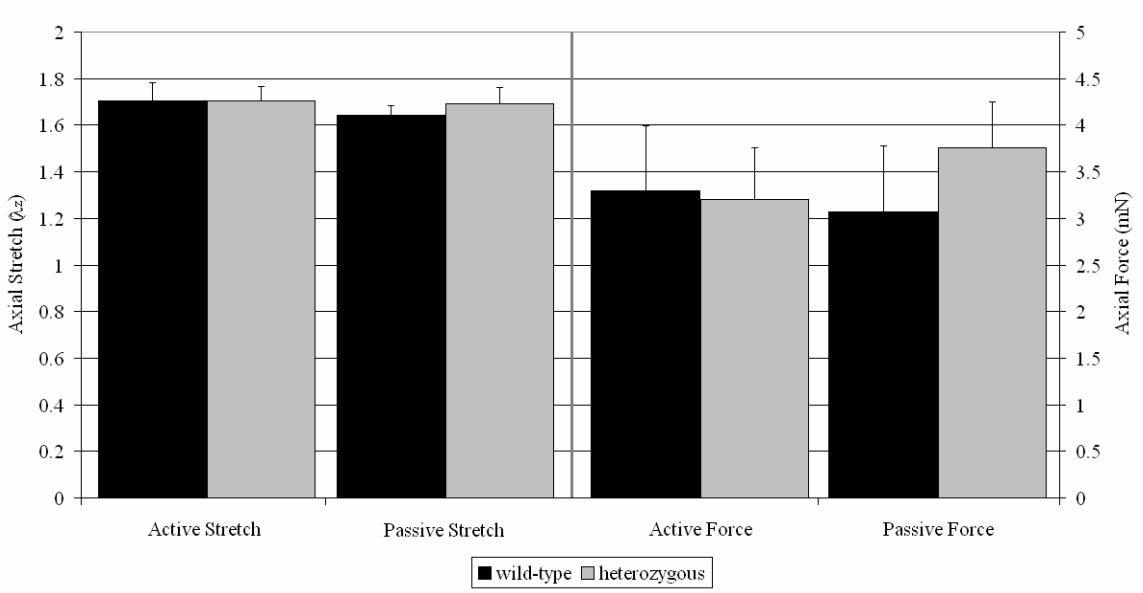

Fig. 12. Averaged active and passive axial *in vivo* stretches and forces.

Table 2
Comparisons of active and passive *in vivo* stretches and forces for wild-type and heterozygous mgR mice.

	Active		**Passive**	
	Wild-Type	**Heterozygous**	**Wild-Type**	**Heterozygous**
$\lambda_{z\ in\ vivo}$	1.706 ± 0.077	1.704 ± 0.062	1.645 ± 0.040	1.694 ± 0.067
***f* at $\lambda_{z\ in\ vivo}$ (mN)**	3.301 ± 0.693	3.200 ± 0.558	3.072 ± 0.707	3.762 ± 0.488

All data are represented as mean ± standard deviation.

Discussion

Given that mice heterozygous for the mgR construct are not phenotypically different from wild-type controls (Pereira et al., 1999), it was not surprising that the majority of the pressure-diameter, force-pressure, circumferential stress-stretch, axial force-stretch, and axial stress-stretch data were not significantly different in either in the passive state or with basal tone. Nevertheless, several non-statistically significant trends can be seen in the pressure-diameter test data. Specifically, the heterozygous data tend to have smaller diameters than the wild-type curves at physiological pressures and the heterozygous circumferential stress strain curves tend to be shifted to the left of the wild-type curves. Thus, the heterozygous vessels seem slightly less compliant than their wild-type counterparts. No similar trends could be seen in the passive data or the axial force-stretch data, which when combined with the slightly larger average basal tone might suggest that the smooth muscle cells are slightly more active in the heterozygous vessels. However, the passive sample size is small, and no trends are observed in the

heterozygous basal tone, making such a suggestion difficult to establish at this time. Further collection of passive data may clarify this question.

While acute mechanical studies can prove useful for determining tissue properties, it is also important to study how those properties change over time. This is generally accomplished with culture experiments, either *in* or *ex vivo*. Although *in vivo* culture studies are fairly simple to perform and can usually be carried out long term, *ex vivo* studies offer superior control, albeit in a setting foreign to the tissue. Our lab group has developed a sophisticated computer controlled vessel culture system capable of controlling both the internal pressurization, axial stretch, and luminal flow (Gleason et al., 2004a). Vessels can thus be studied under different conditions to see how they adapt, offering clues to their internal makeup and unique mechanical properties. However, these *ex vivo* culture studies may fail due to contamination. Appendix C describes several cleaning protocols used in the lab to combat contamination, decreasing the time and effort necessary to collect data. Future work on Marfan model mice in this lab will undoubtedly involve culture tests to deduce the effects of hypertension on the mechanics and biology of the Marfan vasculature.

Because heterozygous mgR mice have not been extensively studied, the results of surgical or pharmacological intervention are currently unknown. Surgical procedures such as aortic banding or carotid ligation may cause Marfan-like lesions to develop, as might drug-induced hypertension. Further, all the mice tested in this study, although mature adults, were fairly young, and mice heterozygous for mgR have not been studied in advanced age, and thus the time-course of their aging process is currently unknown. It

may be that as the mgR vasculature ages, it may be more prone to Marfan symptoms, in addition to the typical stiffening and elastic fiber calcification that occur with age (Avolio et al., 1983; Bunton et al., 2001).

While the two groups studied were not significantly different, they proved qualitatively different from mice studied previously. Wendy Dye quantified the biomechanical responses of two models of muscular dystrophy and compared them to a wild-type control (C57) in her 2005 thesis. The two models, mdx and sgcd, lack portions of the dystrophin-glycoprotein complex, which connects the cytoskeleton to the extracellular matrix through a number of transmembrane and intracellular proteins and glycoproteins. She found that both the mdx and sgcd strains generally exhibited stiffer behavior in the axial and circumferential directions than wild-types and that the knockouts had a decreased *in vivo* stretch when compared to controls. Although the mechanical data found by Dye were qualitatively different than the data analyzed in this thesis, the functional response and vessel properties were different as well. These findings may be expected when taken in light of a recent paper discussing the effect of mouse strain on vascular remodeling (Harmon et al., 2000). The researchers ligated the left common carotid in eleven in-bred mouse strains, allowed the vasculature to remodel, and then removed the left and right common carotids for morphometric analysis. They found that the strains, which included C57BL/6J and 129/SvJ, varied in their formation of neo-intimal lesions, medial hypertrophy, and their ability to reduce their lumen diameter in response to decreased flow. This paper, together with the data collected by

Dye, suggest that the hybrid background of the animals in this study results in vessels with unique physical and biomechanical properties.

One such important property is the *in vivo* axial stretch. It is known that blood vessels are extended far beyond their unloaded length *in vivo*, and that at the *in vivo* axial stretch the axial force tends to remain constant over a range of pressures (Humphrey, 2002). Previous studies have estimated the *in vivo* stretches for wild-type FVB/N, wild-type C57, and the two models of muscular dystrophy mentioned above (Gleason et al., 2006; Dye, 2005). These values ranged from approximately 1.87 and 1.88 for the FVB/N and C57 groups, respectively, to 1.74 and 1.78 for the mdx and sgcd muscular dystrophy models. The value found in this study for both the heterozygous mgR and wild-type mice was 1.70, substantially lower than both the controls and disease models studied previously. Presumably this difference in the *in vivo* stretches is due to physical and physiological differences between strains.

Given elastin composes approximately 20 percent (dry weight) of the carotid artery (Gleason et al., 2004b), it is reasonable to assume that elastin plays an important role in vascular biomechanics. Mice heterozygous for the elastin gene have 30 percent less elastin content in the vasculature, as compared to wild-types (C57BL/6J), as well as an increased number of thinner elastic lamina and hypertension (Wagenseil et al., 2005). Wagenseil et al. performed inflation and extension tests on several major vessels (the ascending aorta, abdominal aorta, and common carotid) from both wild-type and elastin-deficient mice and found that the elastin-deficient vessels were less compliant, had smaller diameters, and smaller *in vivo* stretches than wild-types. The *in vivo* stretch the

elastin-deficient carotids was approximately 1.3, although the wild-type *in vivo* stretch was approximately 1.45, significantly smaller than that found in our lab, perhaps due to differences in experimental procedure or *in vivo* stretch calculation.

Fibulin-5 interacts with elastic fibers and links them to the cells via integrins (Kelleher et al., 2004). Fibulin-5 is also necessary to tropoelastin deposition and elastic fiber development (Robinson et al., 2006; Kielty et al., 2005). Fibulin-5 deficient mice have disrupted elastin formation, resulting in vascular malformations and narrowing of the proximal aorta (Ramirez et al., 2004). In a study similar to those listed above, Dr. Rudolph Gleason found that carotids from fibulin-5 knockout mice have biomechanical properties similar to those of elastin-deficient vessels. The fibulin-1 null vessels were significantly stiffer than wild-type vessels, and had an *in vivo* stretch of approximately 1.45 verses 1.85 in the wild-type (Gleason, unpublished observations).

In order to model and predict mechanical behavior, the vasculature is often simplified to a bare minimum (Gleason and Humphrey 2004; 2005), but a biological tissue is composed of far more than three or four components, and these components interact with each other in unknown ways. Although the models provide an important first approximation, the subtle interactions between components can only be studied in actual tissues. Studies such as those listed above show a spectrum of phenotypes from diseased to healthy, giving clues about how the vasculature adapts to missing or decreased levels load-bearing proteins such as elastin and fibrillin-1 or proteins which connect cells to the matrix such as dystrophin, sarcoglycan delta, and fibulin-5. These studies demonstrate how cells alter their environment in response to altered mechanical

loads. It is by studying both the mechanics and biological response that we can begin to model the vasculature in both health and disease, allowing clinicians to appropriately predict and treat issues that arise in diseases such as muscular dystrophy and Marfan syndrome, as well as problems developed in the normal aging process.

CONCLUSION AND RECOMMENDATIONS

This study successfully quantified the active and passive biomechanical responses of both wild-type and heterozygous mgR mouse carotid arteries to inflation and axial stretching tests. Although the two groups did not prove statistically different, they were qualitatively different from other mice studied in our lab and elsewhere. In addition, this study proved conclusively that the heterozygous mgR group is not suitable as a model for Marfan syndrome. However, future protein and RNA analysis, in addition to histological staining, may demonstrate differences that can be exploited through surgical or pharmacological intervention to determine further the effects of graded fibrillin-1 deficiencies.

Future studies should include acute tests on mice homozygous for mgR, as well as two-day normotensive culture tests for wild-type and knockout groups to determine the biomechanical properties of mice with a Marfan phenotype. Further, the culture studies should be repeated at hypertensive pressure to reveal the response of both the wild-type and knockout groups to hypertension. Protein and RNA analysis of the acute knockout, cultured wild-type, and cultured knockout groups, especially regarding the regulation of TGF-β, may also provide clinically relevant data on the physiological changes in Marfan syndrome.

REFERENCES

Aaron, B.B., Gosline, J.M., 1981. Elastin as a random-network elastomer: a mechanical and optical analysis of single elastin fibers. Biopolymers 20, 1247-1260.

Arteaga-Solis, E., Gayraud, B., Ramirez, F., 2000. Elastic and collagenous networks in vascular diseases. Cell Structure and Function 25, 69-72.

Avolio, A.P., Chen, S.G., Wang, R.P., Zhang, C.L., Li, M.F., O'Rourke, M.F., 1983. Effects of aging on changing arterial compliance and left ventricular load in a northern Chinese urban community. Circulation 68, 50-58.

Avolio, A.P., Deng, F.Q., Li, W.Q., Luo, Y.F., Huang, Z.D., Xing, L.F., O'Rourke, M.F., 1985. Effects of aging on arterial distensibility in populations with high and low prevalence of hypertension: comparison between urban and rural communities in China. Circulation 71, 202-210.

Baldock, C., Koster, A.J., Ziese, U., Rock, M.J., Sherratt, M.J., Kadler, K.E., Shuttleworth, C.A., Kielty, C.M., 2001. The supramolecular organization of fibrillin-rich microfibrils. Journal of Cell Biology 152, 1045-1056.

Bellingham, C.M., Woodhouse, K.A., Robson, P., Rothstein, S.J., Keeley, F.W., 2001. Self-aggregation characteristics of recombinantly expressed human elastin polypeptides. Biochimica et Biophysica Acta 1550, 6-19.

Bunton, T.E., Biery, N.J., Myers, L., Gayraud, B., Ramirez, F., Dietz, H.C., 2001. Phenotypic alteration of vascular smooth muscle cells precedes elastolysis in a mouse model of Marfan syndrome. Circulation Research 88, 37-43.

Cardy, C.M., Handford, P.A., 1998. Metal ion dependency of microfibrils supports a rod-like conformation for fibrillin-1 calcium-binding epidermal growth factor-like domains. Journal of Molecular Biology 276, 855-860.

Carta, L., Pereira, L., Arteaga-Solis, E., Lee-Arteaga, S.Y., Lenart, B., Starcher, B., Merkel, C.A., Sukoyan, M., Kerkis, A., Hazeki, N., Keene, D.R., Sakai, L.Y., Ramirez, F., 2006. Fibrillins 1 and 2 perform partially overlapping functions during aortic development. Journal of Biological Chemistry 281, 8016-8023.

Carton, R.W., Dainauskas, J., Clark, J.W., 1962. Elastic properties of single elastic fibers. Journal of Applied Physiology 17, 547-551.

Charbonneau, N.L., Ono, R.N., Corson, G.M., Keene, D.R., Sakai, L.Y., 2004. Fine tuning of growth factor signals depends on fibrillin microfibril networks. Birth Defects Research. Part C, Embryo Today 72, 37-50.

Davis, E.C., 1993. Endothelial cell connecting filaments anchor endothelial cells to the subjacent elastic lamina in the developing aortic intima of the mouse. Cell and Tissue Research 272, 211-219.

Davis, E.C., 1994. Immunolocalization of microfibril and microfibril-associated proteins in the subendothelial matrix of the developing mouse aorta. Journal of Cell Science 107, 727-736.

Davis, E.C., Roth, R.A., Heuser, J.E., Mecham R.P., 2002. Ultrastructural properties of ciliary zonule microfibrils. Journal of Structural Biology 139, 65-75.

Dye, W.W., 2005. Altered biomechanical properties of large arteries in muscular dystrophy. Master of Science Thesis, Texas A&M University, College Station, TX, USA.

Gleason, R.L., Humphrey, J.D., 2004. A mixture model of arterial growth and remodeling in hypertension: altered muscle tone and tissue turnover. Journal of Vascular Research 41, 352-363.

Gleason, R.L., Humphrey J.D., 2005. Effects of a sustained extension on arterial growth and remodeling: a theoretical study. Journal of Biomechanics 38, 1255-1261.

Gleason, R.L., Gray, S.P., Wilson, E., Humphrey, J.D, 2004a. A multiaxial computer-controlled organ culture and biomechanical device for mouse carotid arteries. ASME Journal of Biomechanical Engineering 126, 787-795.

Gleason, R.L., Taber, L.A., Humphrey, J.D., 2004b. A 2-D model of flow-induced alterations in the geometry, structure, and properties of carotid arteries. ASME Journal of Biomechanical Engineering.126, 371-381.

Gleason, R.L., Wilson, E., Humphrey, J.D., 2006. Biaxial biomechanical adaptations of mouse carotid arteries cultured at altered axial extension. Journal of Biomechanics, in press, doi:10.1016/j.jbiomech.2006.03.018.

Groenink, M., de Roos, A., Mulder, B.J., Spaan, J.A., van der Wall, E.E., 1998. Changes in aortic distensibility and pulse wave velocity assessed with magnetic resonance imaging following beta-blocker therapy in the Marfan syndrome. American Journal of Cardiology 82, 203-208.

Groenink, M., de Roos, A., Mulder, B.J., Verbeeten, B. Jr., Timmermans, J., Zwinderman, A.H., Spaan, J.A., van der Wall, E.E., 2001. Biophysical properties of the normal-sized aorta in patients with Marfan syndrome: evaluation with MR flow mapping. Radiology 219, 535-540.

Habashi, J.P., Judge, D.P., Holm, T.M., Cohn, R.D., Loeys, B.L., Cooper, T.K., Myers, L., Klein, E.C., Liu, G., Calvi, C., Podowski, M., Neptune, E.R., Halushka, M.K., Bedja, D., Gabrielson, K., Rifkin, D.B., Carta, L., Ramirez, F., Huso, D.L., Dietz, H.C., 2006. Losartan, an AT1 antagonist, prevents aortic aneurysm in a mouse model of Marfan syndrome. Science 312, 117-121.

Handford, P., Downing. A.K., Rao, Z., Hewett, D.R., Sykes, B.C., Kielty, C.M., 1995. The calcium binding properties and molecular organization of epidermal growth factor-like domains in human fibrillin-1. Journal of Biological Chemistry 270, 6751-6756.

Harmon, K.J., Couper, L.L., Lindner, V., 2000. Strain-dependent vascular remodeling phenotypes in inbred mice. American Journal of Pathology 156, 1741-1748.

Humphrey, J.D., 2002. Cardiovascular Solid Mechanics: Cells, Tissues and Organs. Springer, New York, pp. 280-282.

Jeremy, R.W., Huang, H., Hwa, J., McCarron, H., Hughes, C.F., Richards, J.G., 1994. Relation between age, arterial distensibility, and aortic dilatation in the Marfan syndrome. American Journal of Cardiology 74, 369-373.

Keene, D.R., Jordan, C.D., Reinhardt, D.P., Ridgway, C.C., Ono, R.N., Corson, G.M., Fairhurst, M., Sussman, M.D., Memoli, V.A., Sakai, L.Y., 1997. Fibrillin-1 in human cartilage: developmental expression and formation of special banded fibers. Journal of Histochemistry and Cytochemistry 45, 1069-1082.

Kelleher, C.M., McLean, S.E., Mecham, R.P., 2004. Vascular extracellular matrix and aortic development. Current Topics in Developmental Biology 62, 153-188.

Kielty, C.M., Shuttleworth, C.A., 1995. Fibrillin-containing microfibrils: structure and function in health and disease. International Journal of Biochemistry and Cell Biology 27, 747-760.

Kielty, C.M., Baldock, C., Lee, D., Rock, M.J., Ashworth, J.L., Shuttleworth, C.A., 2002a. Fibrillin: from microfibril assembly to biomechanical function. Philosophical Transactions of the Royal Society of London. Series B, Biological Sciences 357, 207-217.

Kielty, C.M., Wess, T.J., Haston, L., Ashworth, J.L., Sherratt, M.J., Shuttleworth, C.A., 2002b. Fibrillin-rich microfibrils: elastic biopolymers of the extracellular matrix. Journal of Muscle Research and Cell Motility 23, 581-596.

Kielty, C.M., Sherratt, M.J., Marson, A., Baldock, C., 2005. Fibrillin microfibrils. Advances in Protein Chemistry 70, 405-436.

Kozel, B.A., Wachi, H., Davis, E.C., Mecham, R.P., 2003. Domains in tropoelastin that mediate elastin deposition *in vitro* and *in vivo*. Journal of Biological Chemistry 278, 18491-18498.

Lee, B., Godfrey, M., Vitale, E., Hori, H., Mattei, M.G., Sarfarazi, M., Tsipouras, P., Ramirez, F., Hollister, D.W., 1991. Linkage of Marfan syndrome and a phenotypically related disorder to two different fibrillin genes. Nature 352, 330-334.

MacSweeney, S.T., Skidmore, C., Turner, R.J., Sian, M., Brown, L., Henney, A.M., Greenhalgh, R.M., Powell, J.T., 1996. Unravelling the familial tendency to aneurysmal disease: popliteal aneurysm, hypertension and fibrillin genotype. European Journal of Vascular and Endovascular Surgery 12, 162-166.

Marque, V., Kieffer, P., Gayraud, B., Lartaud-Idjouadiene, I., Ramirez, F., Atkinson, J., 2001. Aortic wall mechanics and composition in a transgenic mouse model of Marfan syndrome. Arteriosclerosis, Thrombosis, and Vascular Biology 21, 1184-1189.

Medley, T.L., Cole, T.J., Gatzka, C.D., Wang, W.Y., Dart, A.M., Kingwell, B.A., 2002. Fibrillin-1 genotype is associated with aortic stiffness and disease severity in patients with coronary artery disease. Circulation 105, 810-815.

Milewicz, D.M., Dietz, H.C., Miller, D.C., 2005. Treatment of aortic disease in patients with Marfan syndrome. Circulation 111, e150-157.

Nelson, L.B., Maumenee, I.H., 1982. Ectopia lentis. Survey of Ophthalmology 27, 143-160.

Neptune, E.R., Frischmeyer, P.A., Arking, D.E., Myers, L., Bunton, T.E., Gayraud, B., Ramirez, F., Sakai, L.Y., Dietz, H.C., 2003. Dysregulation of TGF-β activation contributes to pathogenesis in Marfan syndrome. Nature Genetics 33, 407-411.

Öklü, R., Hesketh, R., 2000. The latent transforming growth factor β binding protein (LTBP) family. Biochemical Journal 352, 601-610.

Pereira, L., Lee, S.Y., Gayraud, B., Andrikopoulos, K., Shapiro, S.D., Bunton, T., Biery, N.J., Dietz, H.C., Sakai, L.Y., Ramirez, F., 1999. Pathogenetic sequence for aneurysm revealed in mice underexpressing fibrillin-1. Proceedings of the National Academy of Sciences of the United States of America 96, 3819-3823.

Powell, J.T., Turner, R.J., Henney, A.M., Miller, G.J., Humphries, S.E., 1997. An association between arterial pulse pressure and variation in the fibrillin-1 gene. Heart 78, 396-398.

Powell, J.T., Turner, R.J., Sian, M., Debasso, R., Länne, T., 2005. Influence of fibrillin-1 genotype on the aortic stiffness in men. Journal of Applied Physiology 99, 1036-1040.

Pyeritz, R.E., 2000. The Marfan syndrome. Annual Review of Medicine 51, 481-510.

Ramirez, F., Pereira, L., 1999. Mutations of extracellular matrix components in vascular disease. Annals of Thoracic Surgery 67, 1857-1858.

Ramirez, F., Rifkin, D.B., 2003. Cell signaling events: a view from the matrix. Matrix Biology 22, 101-107.

Ramirez, F., Sakai, L.Y., Dietz, H.C., Rifkin, D.B., 2004. Fibrillin microfibrils: multipurpose extracellular networks in organismal physiology. Physiological Genomics 19, 151-154.

Reinhardt, D.P., Ono, R.N., Sakai, L.Y., 1997. Calcium stabilizes fibrillin-1 against proteolytic degradation. Journal of Biological Chemistry 272, 1231-1236.

Robb, B.W., Wachi, H., Schaub, T., Mecham, R.P., Davis, E.C., 1999. Characterization of an *in vitro* model of elastic fiber assembly. Molecular Biology of the Cell 10, 3595-3605.

Robinson, P.N., Arteaga-Solis, E., Baldock, C., Collod-Beroud, G., Booms, P., De Paepe, A., Dietz, H.C., Guo, G., Handford, P.A., Judge, D.P., Kielty, C.M., Loeys, B., Milewicz, D.M., Ney, A., Ramirez, F., Reinhardt, D.P., Tiedemann, K., Whiteman, P., Godfrey, M., 2006. The molecular genetics of Marfan syndrome and related disorders. Journal of Medical Genetics 43, 769-787.

Ross, R., Bornstein, P., 1969. The elastic fiber: I. The separation and partial characterization of its macromolecular components. Journal of Cell Biology 40, 366-381.

Sachdev, N., Wakefield, D., Coroneo, M.T., 2003. Lens dislocation in Marfan syndrome and UV-B light exposure. Archives of Ophthalmology 121, 585.

Sachdev, N.H., Coroneo, M.T., Wakefield, D., Hennessy, M.P., 2004. Isolated ectopia lentis: potential role of matrix metalloproteinases in fibrillin degradation. Archives of Ophthalmology 122, 111-114.

Sakai, L.Y., Keene, D.R., Engvall, E., 1986. Fibrillin, a new 350-kD glycoprotein, is a component of extracellular microfibrils. Journal of Cell Biology 103, 2499-2509.

Sherratt, M.J., Baldock, C., Haston, J.L., Holmes, D.F., Jones, C.J., Shuttleworth, C.A., Wess, T.J., Kielty, C.M., 2003. Fibrillin microfibrils are stiff reinforcing fibres in compliant tissues. Journal of Molecular Biology 332, 183-193.

Wagenseil, J.E., Nerurkar, N.L., Knutsen, R.H., Okamoto, R.J., Li, D.Y., Mecham, R.P., 2005. Effects of elastin haploinsufficiency on the mechanical behavior of mouse arteries. American Journal of Physiology-Heart and Circulatory Physiology 289, 1209-1217.

Wu-Chen, W.Y., Letson, R.D., Summers, C.G., 2005. Functional and structural outcomes following lensectomy for ectopia lentis. Journal of American Association for Pediatric Ophthalmology and Strabismus 9, 353-357.

Zhang, H., Apfelroth, S.D., Hu, W., Davis, E.C., Sanguineti, C., Bonadio, J., Mecham, R.P., Ramirez, F., 1994. Structure and expression of fibrillin-2, a novel microfibrillar component preferentially located in elastic matrices. Journal of Cell Biology 124, 855-863.

Zhang, H., Hu, W., Ramirez, F., 1995. Developmental expression of fibrillin genes suggests heterogeneity of extracellular microfibrils. Journal of Cell Biology 129, 1165-1176.

APPENDIX A

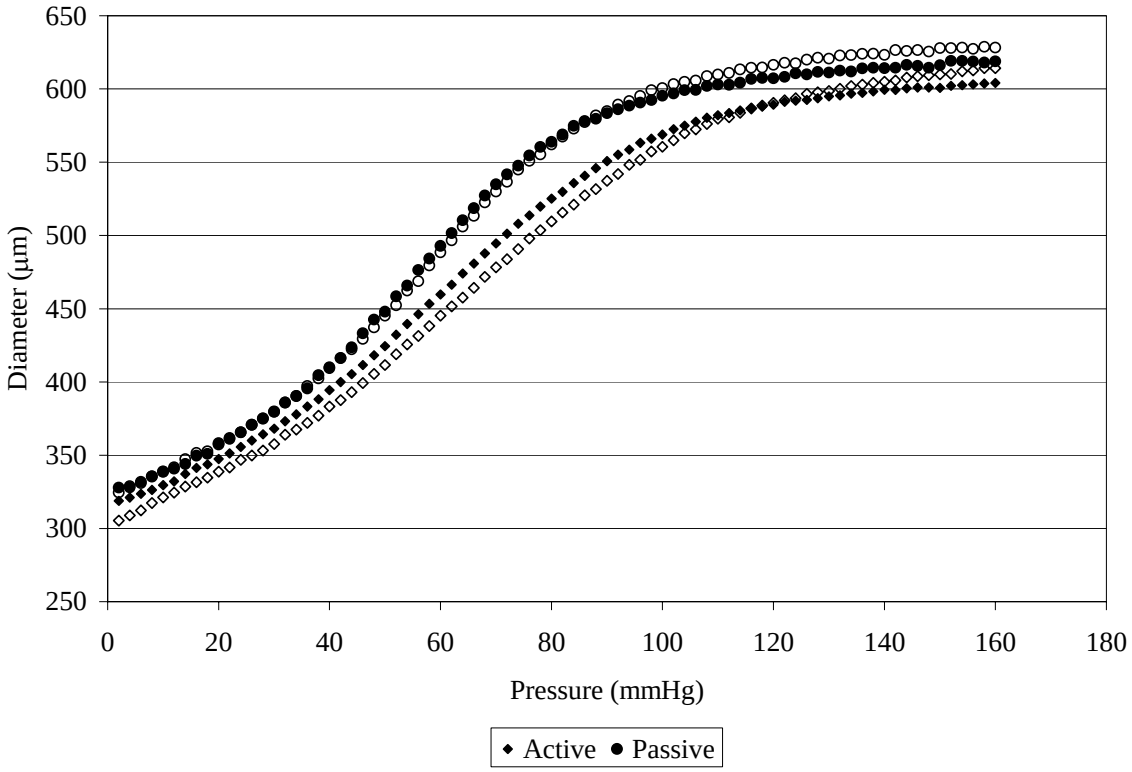

Fig. 13. Averaged pressure-diameter curves at an axial stretch of 1.65. Wild-type curves are denoted by solid symbols, heterozygous curves by hollow symbols.

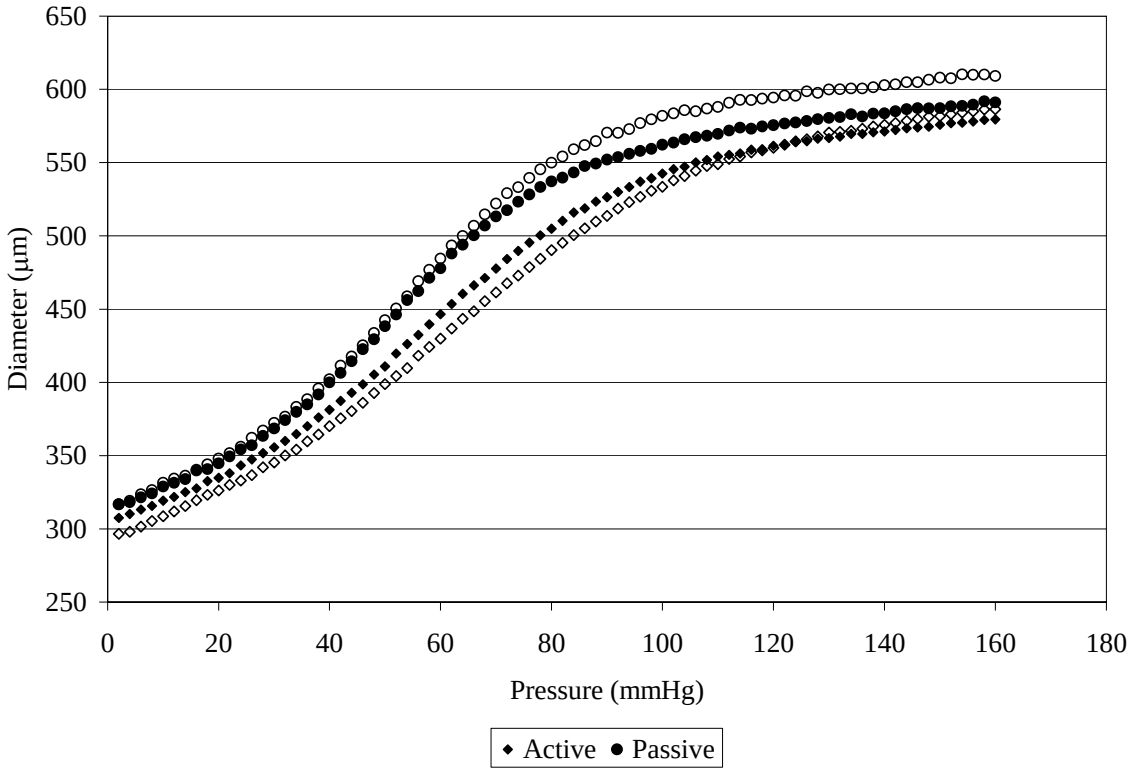

Fig. 14. Averaged pressure-diameter curves at an axial stretch of 1.75. Wild-type curves are denoted by solid symbols, heterozygous curves by hollow symbols.

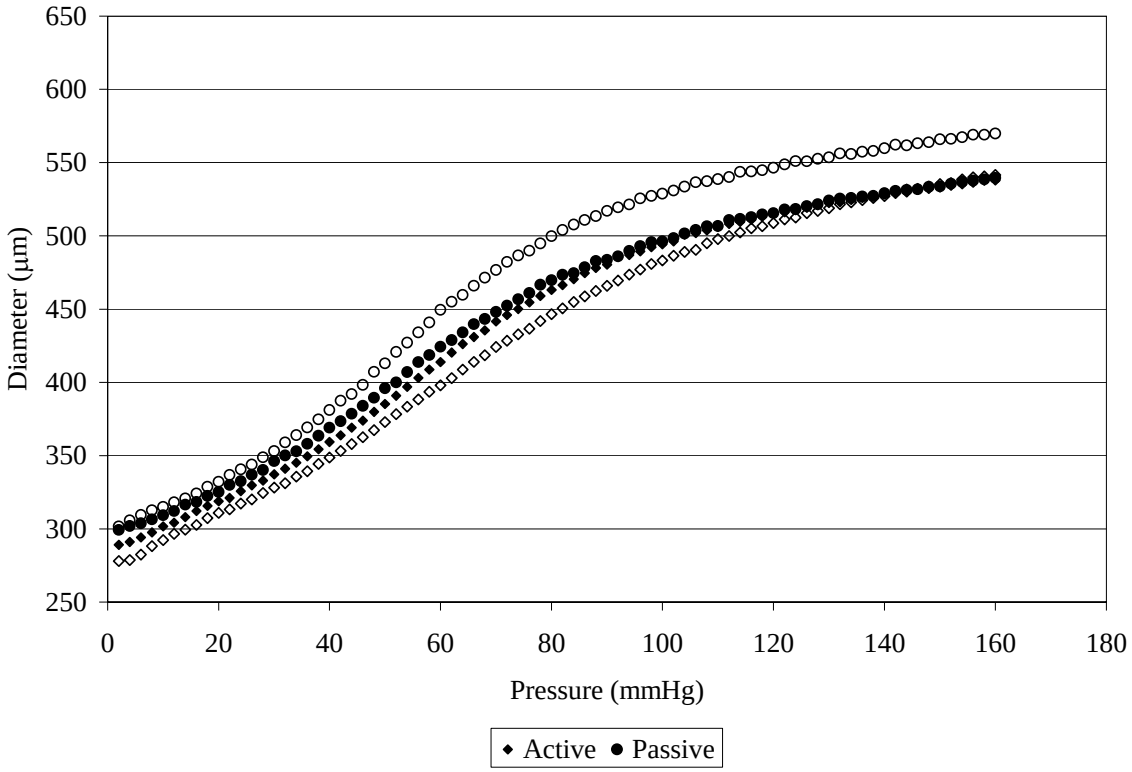

Fig. 15. Averaged pressure-diameter curves at an axial stretch of 1.85. Wild-type curves are denoted by solid symbols, heterozygous curves by hollow symbols.

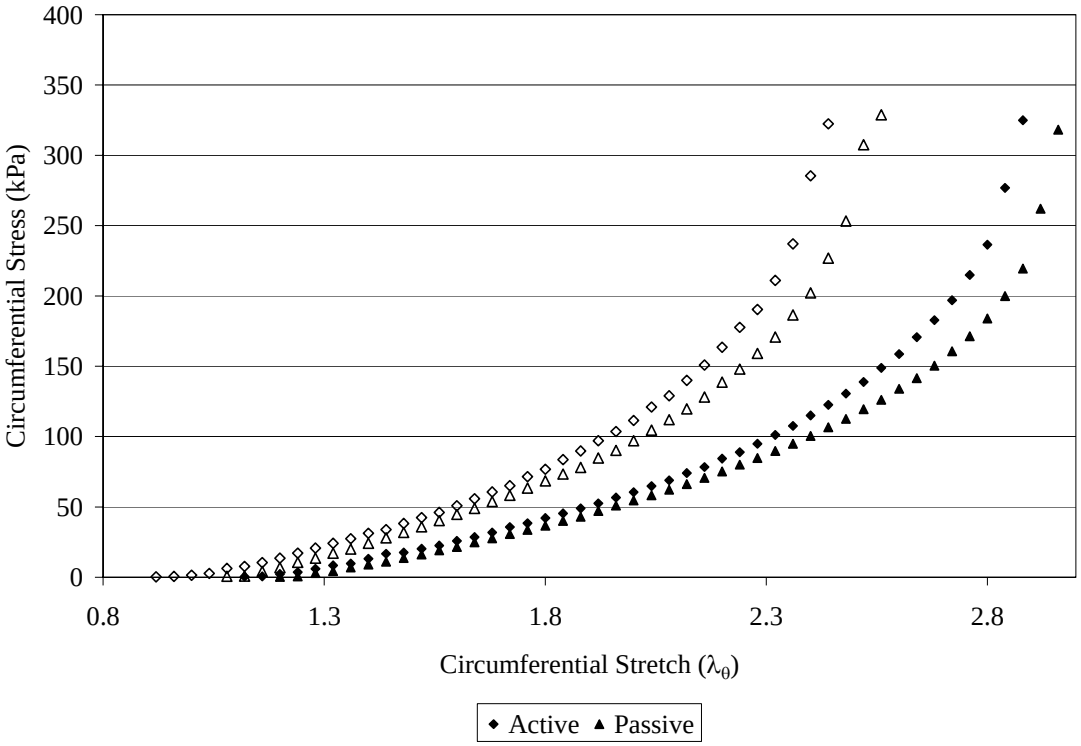

Fig. 16. Representative circumferential stress-stretch curves at an axial stretch of 1.65. Wild-type curves are denoted by solid symbols, heterozygous curves by hollow symbols.

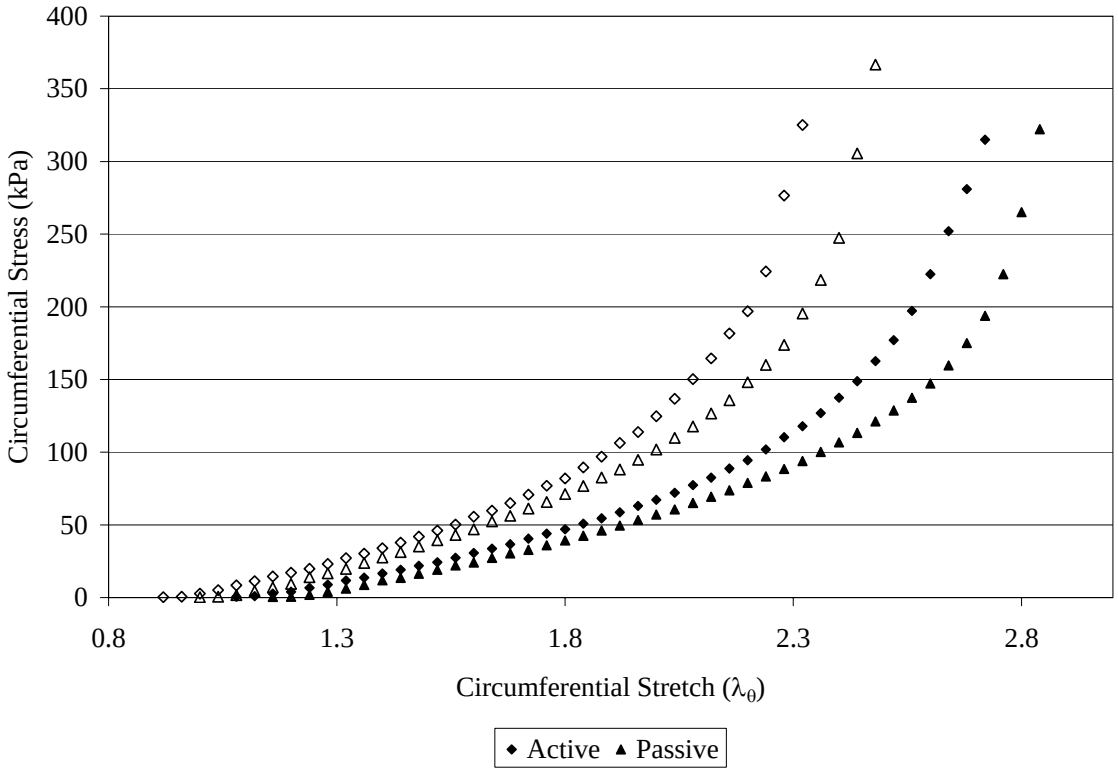

Fig. 17. Representative circumferential stress-stretch curves at an axial stretch of 1.75. Wild-type curves are denoted by solid symbols, heterozygous curves by hollow symbols.

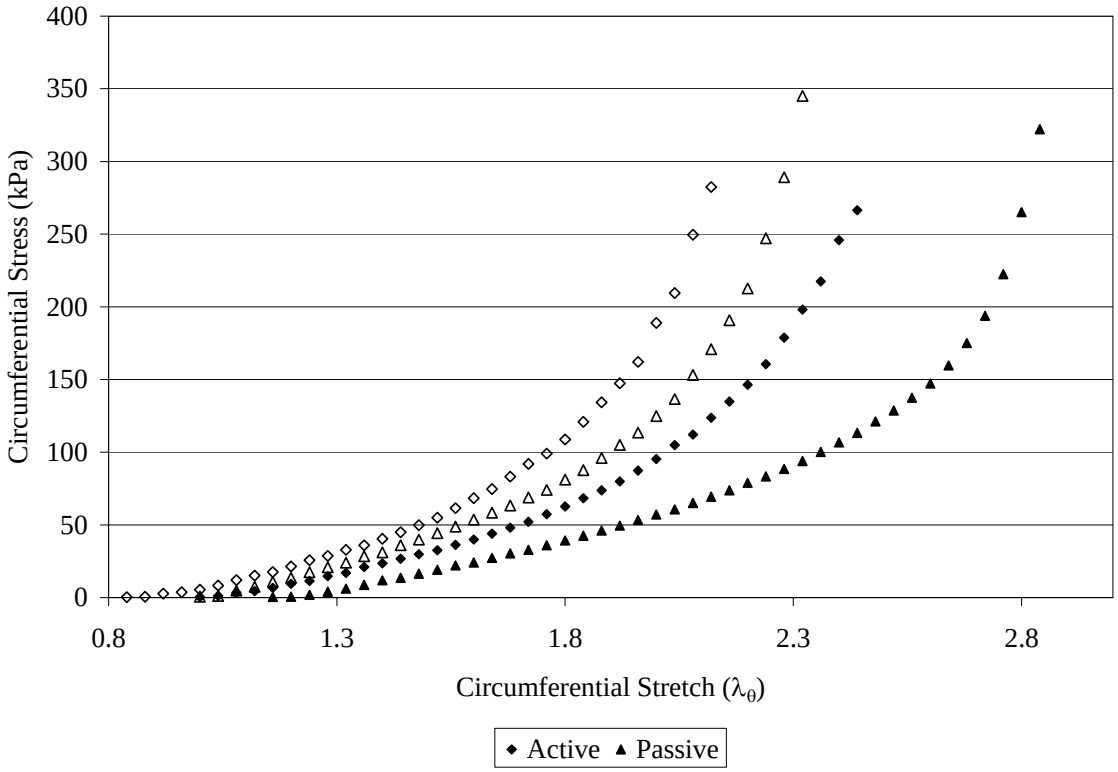

Fig. 18. Representative circumferential stress-stretch curves at an axial stretch of 1.85. Wild-type curves are denoted by solid symbols, heterozygous curves by hollow symbols.

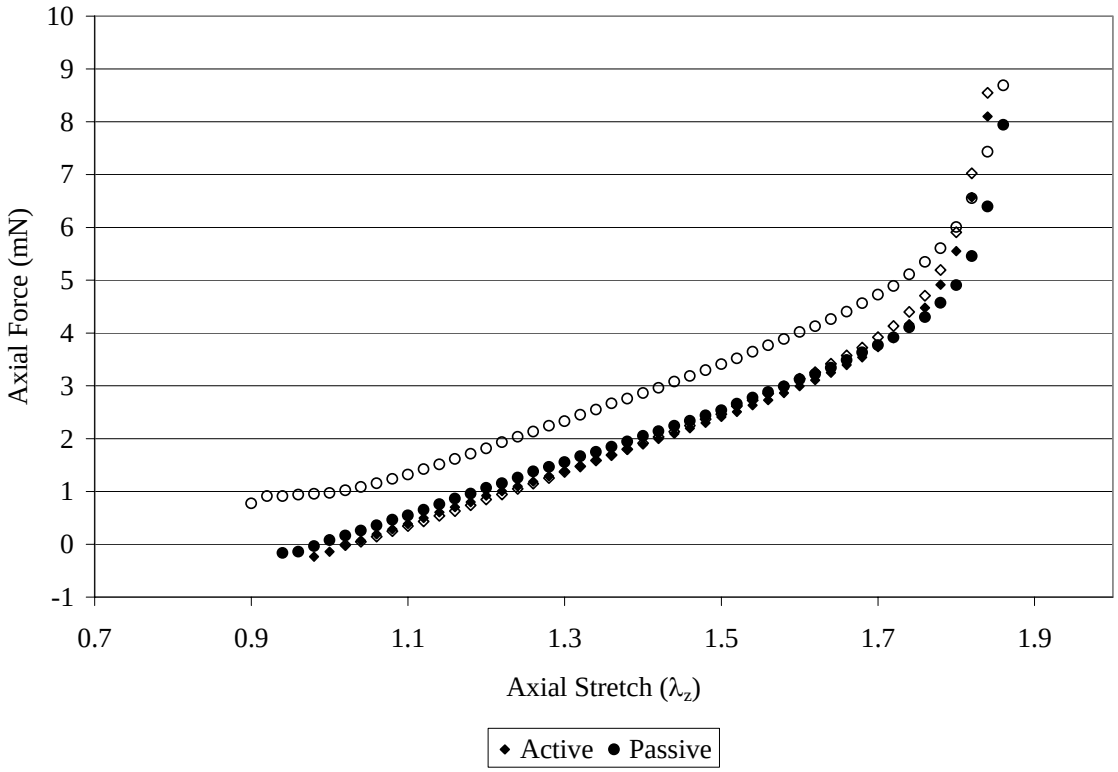

Fig. 19. Representative axial force-stretch curves at a pressure of 0 mmHg. Wild-type curves are denoted by solid symbols, heterozygous curves by hollow symbols.

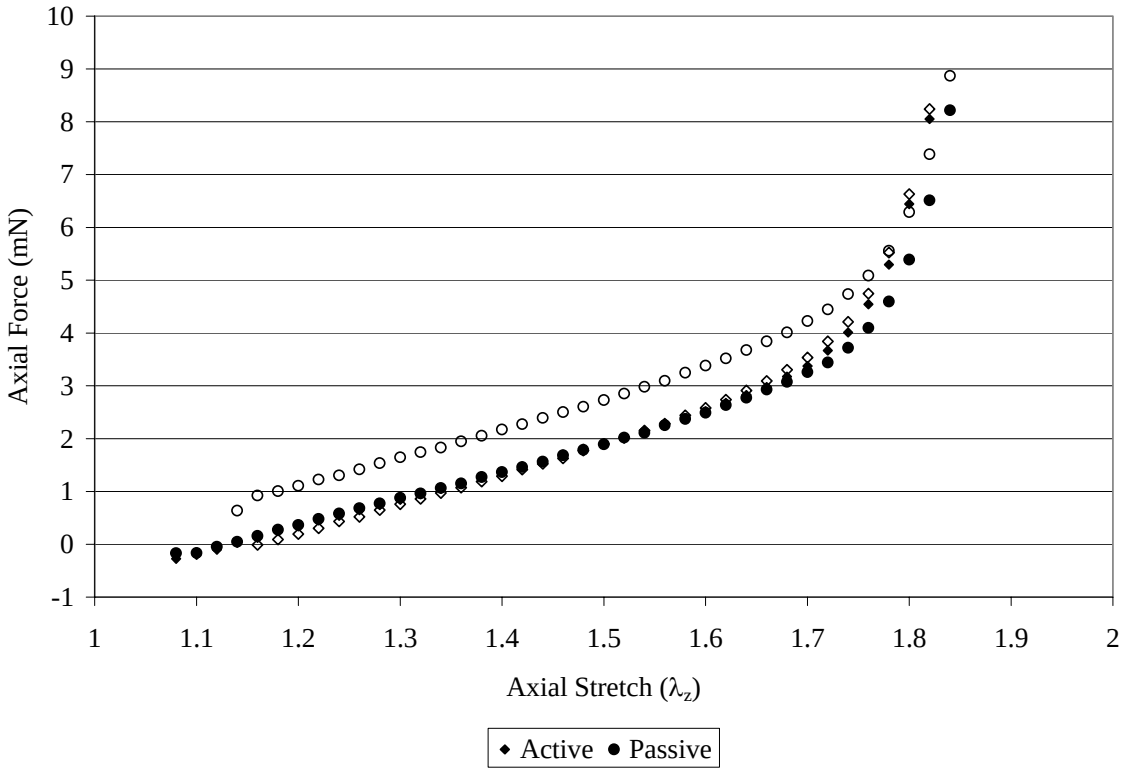

Fig. 20. Representative axial force-stretch curves at a pressure of 60 mmHg. Wild-type curves are denoted by solid symbols, heterozygous curves by hollow symbols.

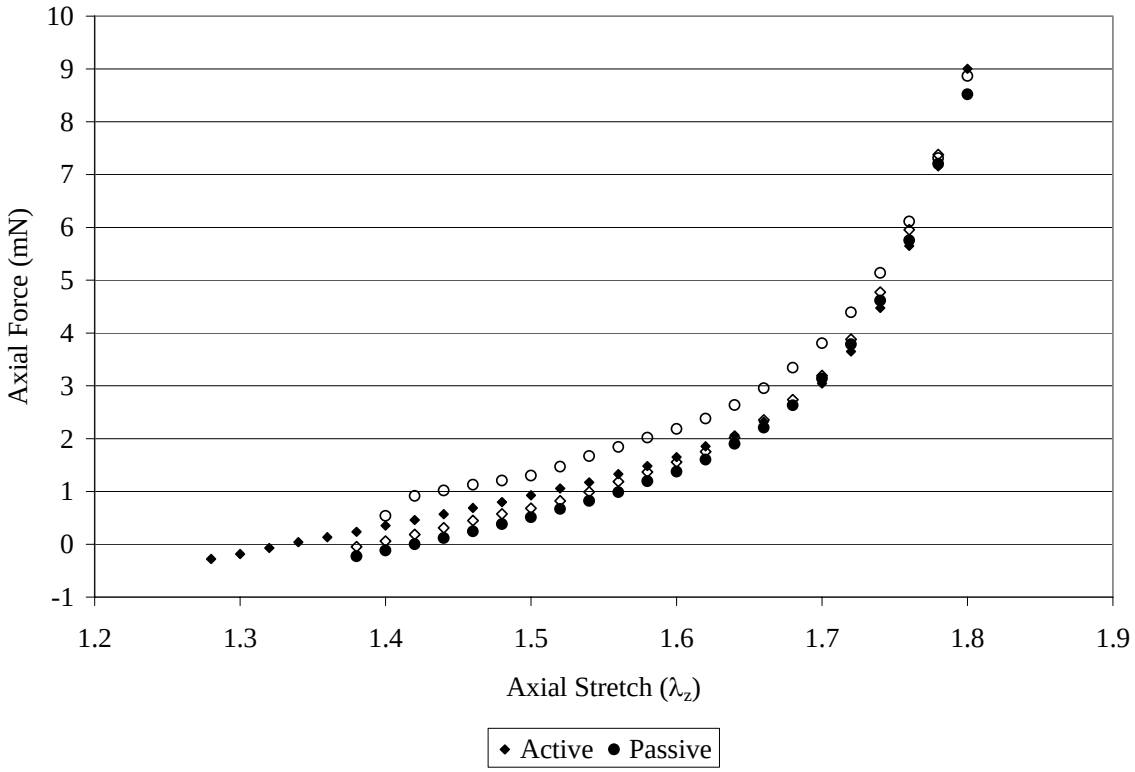

Fig. 21. Representative axial force-stretch curves at a pressure of 100 mmHg. Wild-type curves are denoted by solid symbols, heterozygous curves by hollow symbols.

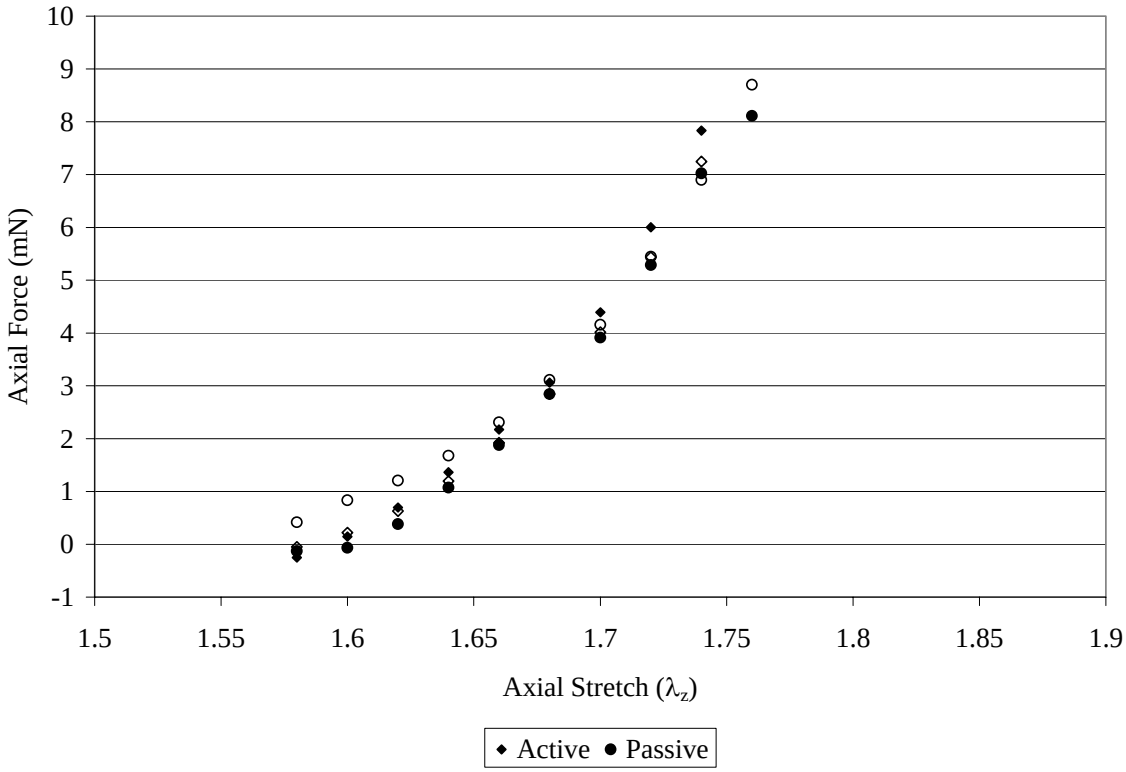

Fig. 22. Representative axial force-stretch curves at a pressure of 160 mmHg. Wild-type curves are denoted by solid symbols, heterozygous curves by hollow symbols.

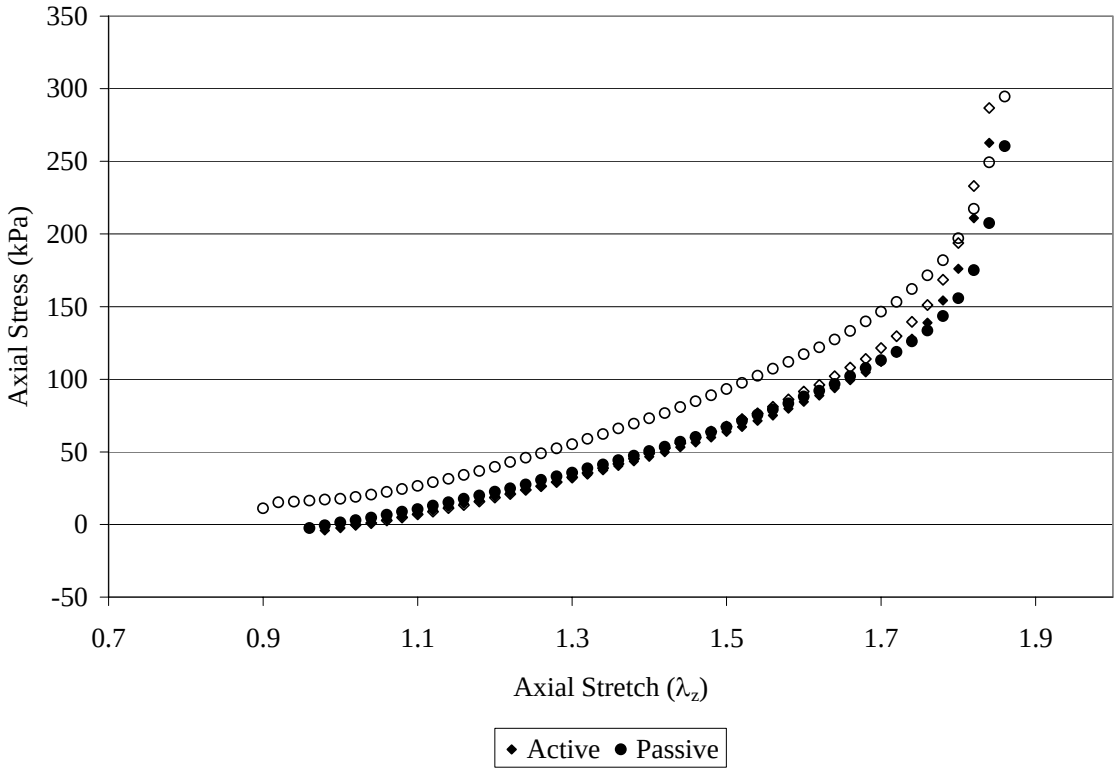

Fig. 23. Representative axial stress-stretch curves at a pressure of 0 mmHg. Wild-type curves are denoted by solid symbols, heterozygous curves by hollow symbols.

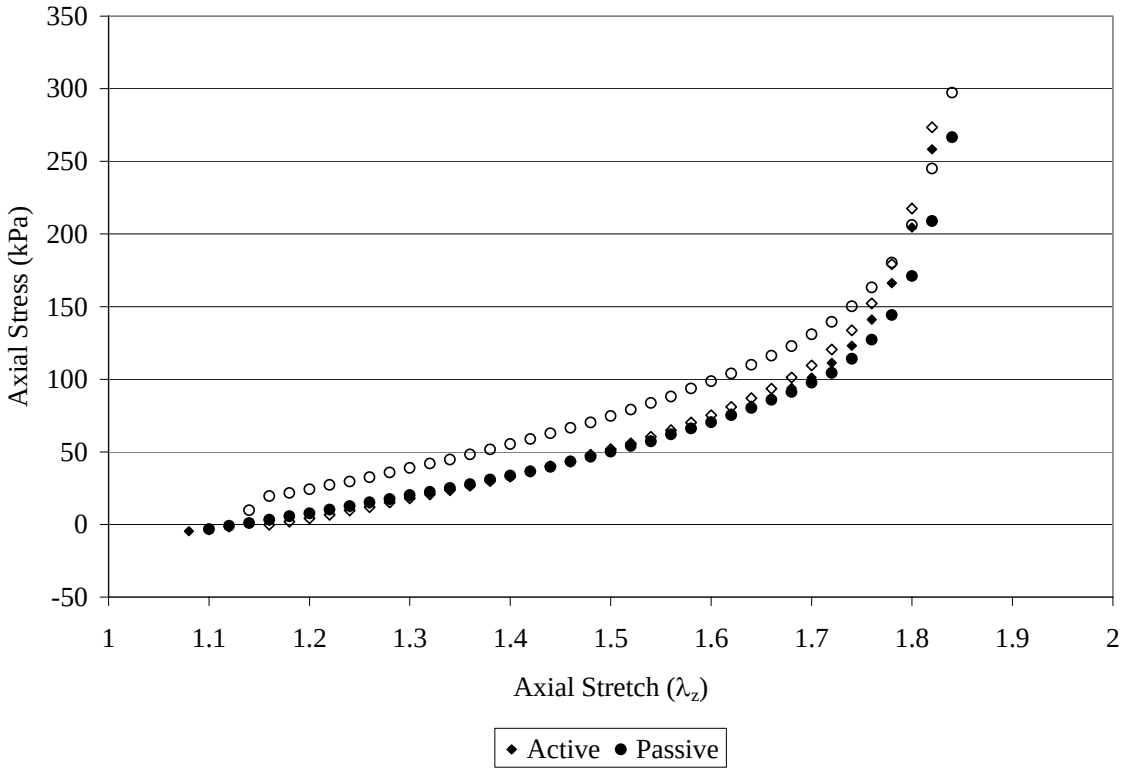

Fig. 24. Representative axial stress-stretch curves at a pressure of 60 mmHg. Wild-type curves are denoted by solid symbols, heterozygous curves by hollow symbols.

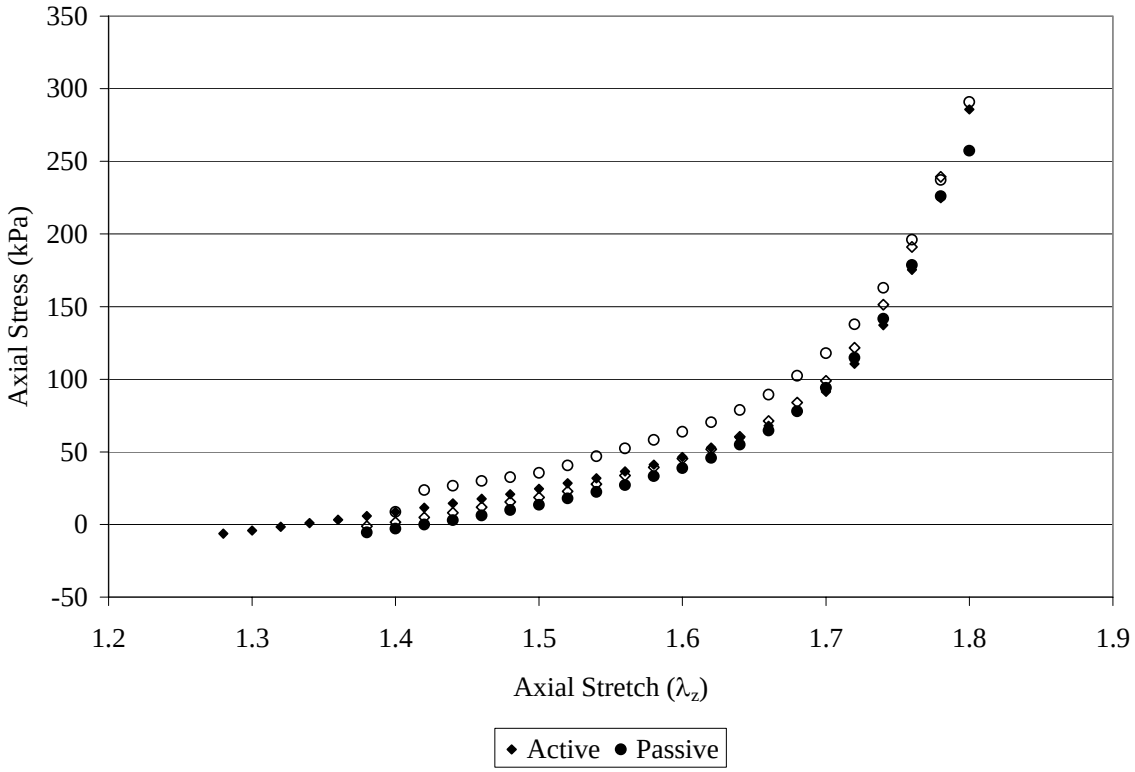

Fig. 25. Representative axial stress-stretch curves at a pressure of 100 mmHg. Wild-type curves are denoted by solid symbols, heterozygous curves by hollow symbols.

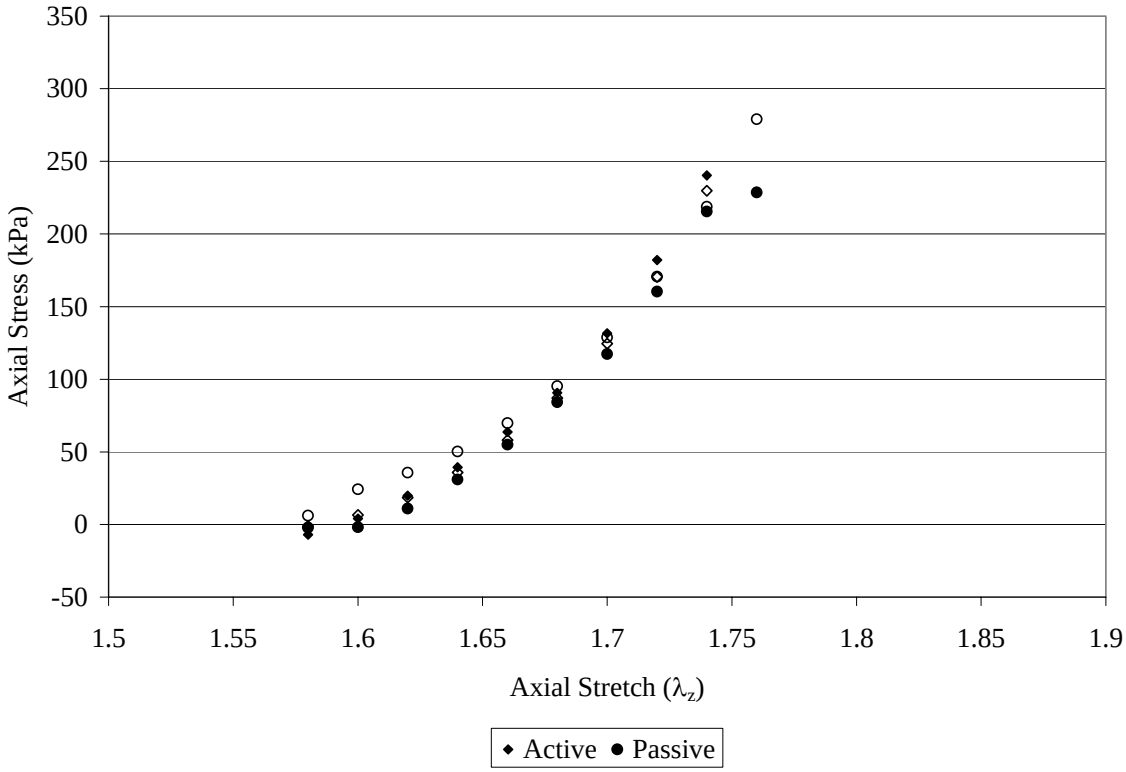

Fig. 26. Representative axial stress-stretch curves at a pressure of 160 mmHg. Wild-type curves are denoted by solid symbols, heterozygous curves by hollow symbols.

APPENDIX B

This visual basic macro code interpolates between unevenly spaced data points. In this case, the program interpolates the diameter and force from collected pressure-diameter test data for a specified table of pressure values

Creates pressure "lookup table"

```
Range("J1500").Select
ActiveCell.FormulaR1C1 = "1"
Range("J1500").Select
Selection.AutoFill Destination:=Range("J1500:J1589"), Type:=xlFillDefault
Range("K1500").Select
ActiveCell.FormulaR1C1 = "2"
Range("K1501").Select
ActiveCell.FormulaR1C1 = "4"
Range("K1500:K1501").Select
Selection.AutoFill Destination:=Range("K1500:K1579"), Type:=xlFillDefault
```

Does the interpolation

```
Columns("J:S").Select
Selection.Sort Key1:=Range("K1"), Order1:=xlAscending, Header:=xlGuess, _
   OrderCustom:=1, MatchCase:=False, Orientation:=xlTopToBottom
Range("M2").Select
ActiveCell.FormulaR1C1 = "=((R[1]C[-1]-R[-1]C[-1])/(R[1]C11-R[-
  1]C11)*RC11+(R[1]C[-1]-(R[1]C[-1]-R[-1]C[-1])/(R[1]C11-R[-1]C11)*R[1]C11))"
Range("M2").Select
Selection.AutoFill Destination:=Range("M2:M1500"), Type:=xlFillDefault
Range("P2").Select
ActiveCell.FormulaR1C1 = "=((R[1]C[-1]-R[-1]C[-1])/(R[1]C11-R[-
  1]C11)*RC11+(R[1]C[-1]-(R[1]C[-1]-R[-1]C[-1])/(R[1]C11-R[-1]C11)*R[1]C11))"
Range("P2").Select
Selection.AutoFill Destination:=Range("P2:P1500"), Type:=xlFillDefault
Columns("M:M").Select
Selection.Copy
Columns("N:N").Select
Selection.PasteSpecial Paste:=xlValues, Operation:=xlNone, SkipBlanks:= _
   False, Transpose:=False
Columns("P:P").Select
Application.CutCopyMode = False
Selection.Copy
Columns("Q:Q").Select
Selection.PasteSpecial Paste:=xlValues, Operation:=xlNone, SkipBlanks:= _
   False, Transpose:=False
Columns("S:S").Select
```

```
Selection.Insert Shift:=xlToRight
Selection.Insert Shift:=xlToRight
Range("S2").Select
ActiveCell.FormulaR1C1 = "=((R[1]C[-1]-R[-1]C[-1])/(R[1]C11-R[-
  1]C11)*RC11+(R[1]C[-1]-(R[1]C[-1]-R[-1]C[-1])/(R[1]C11-R[-1]C11)*R[1]C11))"
Range("S2").Select
Selection.AutoFill Destination:=Range("S2:S1500"), Type:=xlFillDefault
Columns("S:S").Select
Application.CutCopyMode = False
Selection.Copy
Columns("T:T").Select
Selection.PasteSpecial Paste:=xlValues, Operation:=xlNone, SkipBlanks:= _
    False, Transpose:=False
Columns("J:U").Select
Application.CutCopyMode = False
Selection.Sort Key1:=Range("J1"), Order1:=xlAscending, Header:=xlGuess, _
            OrderCustom:=1, MatchCase:=False, Orientation:=xlTopToBottom
```

APPENDIX C

This appendix describes protocols developed to prevent contamination when culturing vessels.

General Maintenance

- Fill pressure transducers with 70% ethanol and cover with foil during storage. Refresh ethanol at least weekly.

Set Up

- Autoclave small-caliber tubing for 1 hour, 15 minutes. Larger caliber tubing may be autoclaved for the same amount of time.
- Rinse pressure transducers with 70% ethanol twice in the laminar flow hood
- Put loops together under laminar flow hood

Deconstructing Loops

- Remove luminal loop first. Remove pressure transducers (unscrewing connector for device 1, P1), remove all remaining PTFE tape, rinse the transducer wells with soap until no more media is seen, and then fill with Alconox until everything else is cleaned. Do not allow electrical connections to get wet.
- Remove filters and attached tubing from reservoirs. Dispose of all clogged filters and check tubing for media deposits. Clean tubing if necessary.
- Rinse interior of all media-contacting tubing with hot water for 10 seconds. Drain and rinse with distilled water for 10 seconds. Drain tubing and allow to dry before autoclaving.
- Squirt Alconox into all openings of reservoirs. Rinse thoroughly with hot water, then with distilled water. Repeat for stoppers.
- Rinse pressure transducers briefly with hot water. Squirt distilled water into pressure transducer until the water is no longer has soapy bubbles. Tap to release trapped bubbles and ensure thorough rinsing. Rinse twice with 70% ethanol, tapping to release bubbles, and store as described above.

Cleaning to Remove Bacteria

- Clean as above, except squirt soap into all tubing that contacts media. Rinse thoroughly with hot water to remove soap.
- If film forms in the reservoir, remove with brush and soap.
- If contamination returns, despite cleaning tubing with soap, dispose of tubing and fittings and replace with fresh materials.

Cleaning to Remove Fungus/Mold

- Do not leave the loops up longer than six weeks.
- Remove clumps of fungus in reservoir with brush and soap. Pay careful attention to spouts.
- Permanent staining of tubing interior and fittings is probable. Some loops may be rescued by cleaning as for bacterial contamination. However, it is often less frustrating to dispose of all tubing and fittings and replace them with fresh materials.

VITA

ANNE IRENE TAUCER
Department of Biomedical Engineering
337 Zachry Engineering Center, 3120 TAMU
College Station, TX, 77843-3120
Email: ataucer@gmail.com

Education

Texas A&M University, College Station, TX

- Master of Science, Biomedical Engineering, December 2006
  GPR 3.875/4.0
- Bachelor of Science, Biomedical Engineering, May 2004
  GPR 3.778/4.0

Research Experience

Research Assistant, advisor Dr. Jay Humphrey — June 2004-present
Department of Biomedical Engineering, Texas A&M University

Student Technician, supervisor Dr. Michael Davis — Spring 2004
Department of Medical Physiology, Texas A&M University

- Develop LabVIEW program to control and monitor muscle tension in rat arterioles
- Create LabVIEW program to display saved myograph data

Student Researcher, supervisor Dr. John Criscione — Summer 2003
Engineering Academic Programs Office, Texas A&M University
Received Undergraduate Student Research Grant (USRG)

- Designed and built an optical fixture to measure the birefringence of collagen in thin membranes

Abstracts

Davis, M.J., A. Price, A. Gashev, W. Wang, D.C. Zawieja, R. Zhang. Force-Velocity Relationships Of Rat Mesenteric Lymphatics And Arterioles. Experimental Biology 2005; April 2-6; San Diego, CA.

Honors

Tau Beta Pi—General Engineering Honor Society
Delta Phi Alpha—German Honor Society

Undergraduate Activities

Engineering Study Abroad in Germany—Summer 2000
Society of Women Engineers
ASPIRE: Aggie Scholars Promoting Incentive Resources & Encouragement